J. Fluid Mech. (2024), *vol*. 997, A38, doi:10.1017/jfm.2024.606

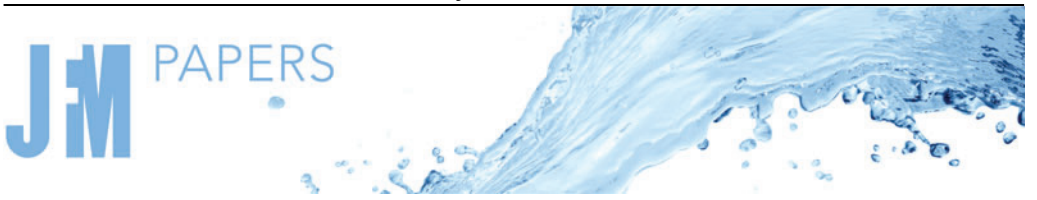

On the linear response theory of vortex meandering and its statistical verification in experiments

Tobias Bölle†

Deutsches Zentrum für Luft- und Raumfahrt, Institut für Physik der Atmosphäre, Oberpfaffenhofen, Germany

(Received 22 March 2024; revised 26 July 2024; accepted 30 July 2024)

Meandering designates the main manifestation of unsteady vortex dynamics observed in experiments. This study has the twofold objective to (i) develop a theoretical model describing vortex meandering and (ii) conduct a quantitative and objective evaluation of the model against experimental data. Based on an analogy with Brownian motion, we derive the theoretical model in the framework of linear response theory. Taking the form of a Langevin equation, our model explains meandering as the competition between external excitation by free-stream perturbations, counteracted by stabilising intrinsic vortex dynamics. As such, it contains the previous approaches to explaining the phenomenon as limiting cases, and clearly highlights their shortcomings. The statistical identification of characteristic regularities in experimental data as well as the assessment of their consistency with theoretical models are important problems in physics. For samples obtained from finite-length records of correlated data, these statistical characteristics are not unique and may show spurious behaviour merely induced by the finiteness of the sample. Statistical inference provides a systematic and quantitative methodology to objectively assess the reproducibility of statistical characteristics and to evaluate their consistency with theoretical models. Their systematic application to the analysis of vortex meandering has not been done before and provides statistical evidence for our proposed Brownian-motion-like model. That is, experimental vortex meandering constitutes the manifestation of a stationary Gauss–Markov random process, which implies that the dynamics admits an ergodic probability measure.

Key words: low-dimensional models, vortex dynamics, vortex instability

† Email address for correspondence: tobias.boelle@dlr.de

1. Introduction

Vortex meandering is the prototype of the slow response dynamics of an isolated line vortex evolving in an environment of weakly-structured disturbances. As such, it is documented to affect a large variety of vortex-dominated flows from engineering to geophysics. Prominent examples include experiments and simulations of trailing vortices (Devenport *et al.* 1996; Jammy, Hills & Birch 2014; Bailey *et al.* 2018), inlet vortices (Wang & Gursul 2012) and tornadoes (Karami *et al.* 2019; Zhang *et al.* 2023). Despite its universal observation in experiments since the 1970s (Corsiglia, Schwind & Chigier 1973; Baker *et al.* 1974), the origin and mechanism of vortex meandering remain puzzling (Edstrand *et al.* 2016; Qiu *et al.* 2021; Bölle 2023).

In essence, past approaches to explain vortex meandering approximately fall into two families, seeking to attribute the meandering dynamics to extrinsic or intrinsic mechanisms, respectively (Bölle 2021). In this regard, early studies seem to be influenced mainly by classical statistical turbulence theory (Tennekes & Lumley 1972). The principal picture that arose from these studies describes meandering as a stochastic error motion of a dynamically passive vortex being perpetually 'beaten' by the surrounding free-stream turbulence (e.g. Corsiglia *et al.* 1973; Baker *et al.* 1974; Devenport *et al.* 1996; Bailey & Tavoularis 2008).

On the other hand, Bandyopadhyay, Stead & Ash (1991) emphasised that 'the vortex core is not a benign solid body of rotation but has a dynamic nature', which was followed by a general paradigm change towards attributing meandering to deterministic dynamics intrinsic to the vortex – essentially as some form of an instability (e.g. Jacquin *et al.* 2001; Fabre, Sipp & Jacquin 2006; Mao & Sherwin 2012). The identification of vortex meandering with an instability mechanism basically relies on two characteristics universally observed in experiments, namely, the monotonic downstream amplification of the meandering amplitude, and the fact that the dominant vortex response spatial pattern obtained from a proper orthogonal decomposition of the experimental fluctuation vorticity qualitatively matches well with marginally stable vortex eigenmodes (Edstrand *et al.* 2016; Qiu *et al.* 2021). However, to the best of the authors' knowledge, experimental realisations of line vortices systematically and consistently correspond to linearly stable conditions (Edstrand *et al.* 2016; Bölle *et al.* 2023).

Recently, Bölle (2021) proposed that meandering corresponds to a Brownian motion of the vortex. Based on this recognition, Bölle (2023) developed a theoretical, stochastic model within the context of linear response theory (de Groot & Mazur 1984). Two aspects of this theory have already been proposed in earlier phenomenological models, namely the Gaussian distribution (Baker *et al.* 1974) and the downstream (z) amplitude growth $\sim\sqrt{z}$ (van Jaarsveld *et al.* 2011). Our approach explains these characteristics and additionally predicts a vortex meandering spectral (correlation) structure that can be compared with experiments. In relation to our previous discussion of the historical development, a Brownian-motion-based model implies that vortex meandering must be the consequence of a combined intrinsic–extrinsic dynamics. Figuratively speaking, the vortex's deterministic own dynamics contributes an intrinsic resistance to perpetual stochastic external excitation (Chandrasekhar 1943).

Our first objective in this study is to provide evidence for the validity of this hypothesis on a physical level. To this end, we propose an alternative derivation of the Brownian-motion-like meandering model on the basis of vortex eigenmodes, unlike the original model development in terms of a Karhunen–Loève expansion of the dynamic flow fields (Holmes, Lumley & Berkooz 1996; Bölle 2023). This more clearly allows a discussion of the relevant mechanisms and previously

proposed models. A comparable model assessment does not seem to have been done so far.

Our suggested model corresponds to the postulate that experimentally observed vortex meandering is the manifestation of a stationary Gauss–Markov process. Relating theory and experiment is highly non-trivial, in general. Thus, the second and main objective of the present study is to introduce a rigorous, systematic and objective approach to assess the validity of theoretical models from comparison with experiment. In particular, all analyses should be fully reproducible on alternative datasets, and provide unambiguous quantitative measures that allow an objective confirmation (or rejection) of the model. Statistical inference constitutes the required methodological frame, providing several well-established tools for our purpose (Cramér 1963; Fuller 1996). Of course, we can never expect observations to fit any theoretical model exactly, all the more as we are limited to finite samples to compute statistics. Given that deviations of the experiment from the model are inevitable in practice, statistical inference allows us to assess their significance and reproducibility on a statistical basis. These questions and the problem of discriminating between deterministic dynamics and stochastic noise are very common in signal processing (Yaglom 1962), economics (Abraham & Ledolter 1983; Hamilton 1994; Fuller 1996) and the atmospheric sciences (von Storch & Zwiers 2003; Wilks 2006). However, as far as we know, systematic use of statistical inference in fluid dynamics experiments is rather untypical and has never been applied to the problem of vortex meandering. By means of a systematic application of these tools, we objectively relate the experimental characteristics to a particular theoretical model for the first time. That is, we show that the experimental dataset under consideration is statistically consistent with the Brownian motion model proposed by Bölle (2023).

The paper is organised as follows. First, in § 2 we briefly review the experiment leading to vortex meandering, and summarise the universal characteristics of the phenomenon. We then develop and discuss a theoretical model in the framework of linear response theory in § 3. This model allows the derivation of characteristics that are amenable to statistical verification in experiments. To this end, we introduce the essential terminology and concepts from statistical inference of importance for this study in § 4. Finally, we discuss the application of these tools to the experimental data in § 5, and conclude the main results in § 6.

2. Review of the experimental basis of vortex meandering

In the first part of this section, we briefly present the experiment underlying this study. Our discussion of the dynamical characteristics in § 1 suggests modelling vortex meandering as a stochastic process. Therefore, we subsequently recall the relevant concepts and terminology from the theory of stochastic processes. Finally, we propose a definition of the phenomenon based on experimentally measurable quantities, and resume the universal meandering characteristics.

2.1. *Outline of the experiment*

In the present study, we rely on a wind tunnel experiment that was conducted at ONERA, the French Aerospace Lab. We only briefly recall the essential elements here, referring to Bölle *et al.* (2023) for a detailed discussion of the set-up and instrumentation.

The vortex is generated by a rectangular wing model with NACA 0012 profile, chord length $c = 0.125$ m and wing span $b = 0.5$ m, which is suspended from the wind tunnel ceiling. The free-stream velocity is set at $U_\infty = 20$ m s^{-1}, yielding the chord-based

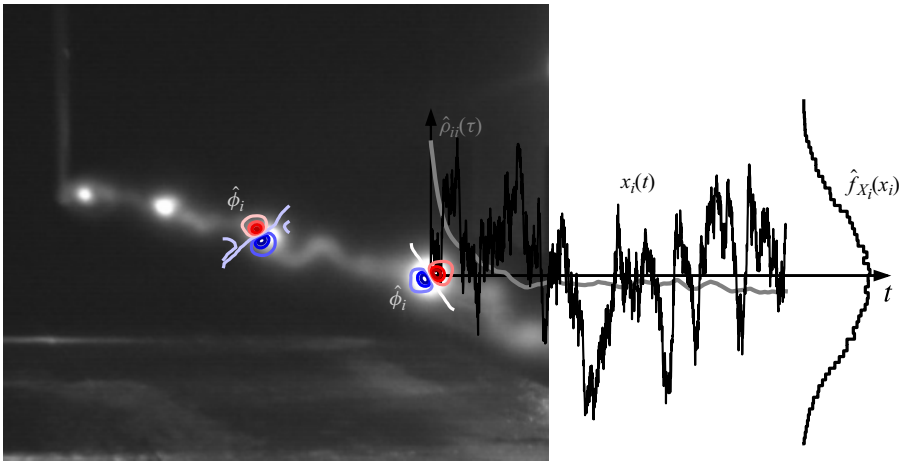

Figure 1. Smoke visualisation of vortex meandering in an experiment (image courtesy Thomas Leweke, IRPHE-CNRS, Marseille, France) and the associated universal principal characteristics in a fixed measurement plane. The variance of the streamwise vorticity component is progressively concentrated in a pair of dipolar patterns (leading proper orthogonal decomposition modes $\hat{\phi}_i(\boldsymbol{r})$, $i = 1, 2$). A sample of the associated principal component $x_i(t)$ over the measurement time t is shown by a black line (arbitrary scaling). These time series are empirically Gaussian distributed $\hat{f}_{X_i}(x_i)$ and have approximately exponential autocorrelation $\hat{\rho}_{ii}(\tau) \approx \exp(-\hat{\lambda}_i \tau)$, where $\hat{\lambda}_i$ denotes the estimated reciprocal vortex response time.

Reynolds number $cU_\infty/\nu \approx 1.7 \times 10^5$. The turbulence intensity in the empty wind tunnel is less than 5×10^{-3}. High-speed stereoscopic particle image velocimetry (PIV) measurements are taken in five transversal measurement planes at constant locations between 2 and 26 chords downstream from the wing. As our interest here is in the temporal dynamics at a fixed downstream position, we restrict to measurements taken in the last plane at 26 chords behind the wing. We denote by $\boldsymbol{r} \in \mathbb{R}^2$ the Cartesian coordinates in this plane centred in the mean vortex-centre position. Images are taken at a sampling frequency $f_s = 3 \times 10^3$ Hz, corresponding to a time step $\Delta t = 3.3 \times 10^{-4}$ s between subsequent measurements. In each measurement run, $N = 4096$ snapshots are recorded, implying a measurement time $T = N\,\Delta t \approx 1.37$ s. The experiment is repeated in ten identically prepared runs.

A snapshot of the meandering vortex in a smoke visualisation realised in another facility by T. Leweke (CNRS-IRPHE, Marseille, France) is shown in figure 1 for illustration. In this perspective view, the vortex, corresponding to the light-grey tubular structure, is generated on the left-hand side and propagates to the right, out of the plane. Meandering denotes the clearly visible lateral displacement of the vortex, thus requiring two independent variables for its characterisation in a fixed measurement plane. The erratic nature of the vortex motion suggests modelling meandering as a bivariate random process, which, provisionally, we refer to as $x_i(t)$, $i = 1, 2$, deferring the definition to § 2.3.

It is generally admitted that vortex meandering is associated with the energy-carrying, slow scales of the vortex dynamics (Devenport *et al.* 1996; Jacquin *et al.* 2001; Roy & Leweke 2008; Bailey *et al.* 2018; Bölle 2021). We therefore apply a low-pass filter to $x_i(t)$ in order to restrict to the governing temporal scales and remove some measurement noise at high frequencies. Inspection of the associated power spectra suggests applying a low-pass filter at a cut-off frequency $f_c = 300$ Hz, i.e. $f_c/f_s = 0.1$ compared with the PIV sampling frequency. The corresponding cut-off period is $\Delta t_c = 1/f_c = 3.3 \times 10^{-3}$ s, or

$\Delta t_c/\Delta t = 10$ in terms of the PIV sampling period. By the Nyquist–Shannon sampling theorem, this implies the highest resolved frequency $f_r \leq 0.5 f_c = \frac{1}{20} f_s = 150$ Hz, or equivalently, periods longer than $\Delta t_r \geq 2\,\Delta t_c = 20\,\Delta t$.

A characteristic statistical time scale associated with a random process is its integral scale, defined as $t_I := \int_0^\infty \mathrm{d}\tau\, \rho(\tau)$, where $\rho(\tau)$ denotes the autocorrelation function in (2.5) below (von Storch & Zwiers 2003). In turbulent flows, t_I is understood to characterise the energy-carrying, slow scales and should therefore be the pertinent scale for vortex meandering (Tennekes & Lumley 1972). From the experimental data, we estimate $\hat{t}_I/\Delta t \approx 10^2$, i.e. the integral scale dynamics is probed about 100 times. In terms of the low-pass filtered data, $\hat{t}_I/\Delta t_c \approx 10$, such that $\hat{t}_I/\Delta t_r \approx 5$. We conclude that the energy-carrying processes of the order of the integral scale are resolved in the experiment.

2.2. *Review of the relevant elements from the theory of stochastic processes*

We recall here some relevant terminology from the theory of stochastic processes; refer to Chandrasekhar (1943), Yaglom (1962) and de Groot & Mazur (1984) for details.

From our discussion of the experiment in § 2.1, we postulate that vortex meandering is described by the bivariate random process $t \mapsto X_i(t)$ $(i = 1, 2)$. If we further assume that vortex meandering is Markovian (cf. §§ 1 and 5), then knowledge of the equilibrium distribution $f(\boldsymbol{x})$ and the transition probability $f(\boldsymbol{x}_0 \,|\, \boldsymbol{x}, t)$ fully characterises the random process. Here, we anticipate that meandering is a stationary process in the measurement time (cf. § 5.3) and assume the existence of an initial state $\boldsymbol{x}_0$ such that also the transition probability is stationary (de Groot & Mazur 1984). This is, of course, consistent with the expected dynamics of an experiment. We thus define the general stochastic moments

$$\overline{g(\boldsymbol{x})}^{eq} = \int_{\mathbb{R}} \mathrm{d}^2x f(\boldsymbol{x})\, g(\boldsymbol{x}), \tag{2.1}$$

$$\overline{g(\boldsymbol{x})}^{\boldsymbol{x}_0}(t) = \int_{\mathbb{R}} \mathrm{d}^2x f(\boldsymbol{x}_0 \,|\, \boldsymbol{x}, t)\, g(\boldsymbol{x}). \tag{2.2}$$

In particular, the expectation and variance are defined by

$$\mu_i(t) = E(X_i(t)) = \overline{x_i}^{\boldsymbol{x}_0}(t) \quad \text{and} \quad \sigma_i^2(t) = V(X_i(t)) = \overline{(x_i - \overline{x_i}^{\boldsymbol{x}_0})^2}^{\boldsymbol{x}_0}(t). \tag{2.3a,b}$$

We suppose that the process is stationary in any fixed measurement plane of § 2.1, and introduce the joint distribution function $F_{X_iX_j}(x_i, x_j; \tau)$, $|\tau| \geq 0$, where i, j denote any two components of $\boldsymbol{X}(t)$ mutually separated by the lag τ. Supposing that the two component processes $X_i(t)$ and $X_j(t)$ $(i, j = 1, 2)$ have zero expectation, the covariance is defined as

$$C_{ij}(\tau) = E(X_i(t)\, X_j(t+\tau)) = \int_{\mathbb{R}^2} x_i x_j \,\mathrm{d}F_{X_iX_j}(x_i, x_j; \tau), \quad |\tau| \geq 0, \tag{2.4}$$

and the cross-correlation follows from normalisation:

$$[-1, 1] \ni \rho_{ij}(\tau) = \frac{E(X_i(t)\, X_j(t+\tau))}{\sigma_i \sigma_j}. \tag{2.5}$$

The Wiener–Khinchin theorem relates the covariance function (2.4) and the power spectrum $G_{ij}(\omega)$ in terms of the Fourier transform pair

$$G_{ij}(\omega) = \frac{1}{2\pi} \int_{\mathbb{R}} \mathrm{d}\tau\, \mathrm{e}^{-\mathrm{i}\omega\tau}\, C_{ij}(\tau), \quad C_{ij}(\tau) = \int_{\mathbb{R}} \mathrm{d}\omega\, \mathrm{e}^{\mathrm{i}\omega\tau}\, G_{ij}(\omega). \tag{2.6a,b}$$

2.3. *Definition of vortex meandering and kinematic–dynamic equivalence*

Meandering denotes the lateral displacement of the vortex core, clearly visible in figure 1, which readily suggests defining vortex meandering as the motion of the vortex centre. To this end, let V be a subset of the measurement plane that contains the vortex core for all times. Then the vortex centre is defined as ($i = 1, 2$)

$$r_{v,i}(t,z) := \frac{1}{\Gamma}\int_V \mathrm{d}^2 r\, r_i\, w(t,z,\boldsymbol{r}), \quad \text{where } \Gamma(t,z) := \int_V \mathrm{d}^2 r\, w(t,z,\boldsymbol{r}) \tag{2.7a,b}$$

denotes the circulation contained in V, and $(t,z) \mapsto w(t,z)$ is the spatiotemporal evolution of the streamwise vorticity component along the measurement section. Equation (2.7*a*,*b*) expresses vortex meandering as the kinematic motion of a geometrical point in space.

In order to obtain a dynamic formulation of the problem, we assume that $(t,z) \mapsto w(t,z)$ is a spatiotemporal random process and apply the Reynolds decomposition $w(t,z,\boldsymbol{r}) = \bar{w}^{eq}(\boldsymbol{r}) + w'(t,z,\boldsymbol{r})$ (de Groot & Mazur 1984). Here, we assume that the mean vorticity $\bar{w}^{eq}(\boldsymbol{r})$ is stationary and homogeneous, and further expand the fluctuation vorticity as $w'(t,z) = \sum_{k=1}^{\infty} x_k(t,z)\,\phi_k(\boldsymbol{r})$, where $\phi_k(\boldsymbol{r})$ are the spatial modes obtained from a proper orthogonal decomposition (POD) of the streamwise component of the fluctuation vorticity (details are given in § 5.1). In figure 1, the typical dipolar pattern of these POD modes is shown by the red–blue contour plots, where $\phi_1(\boldsymbol{r})$ and $\phi_2(\boldsymbol{r})$ are mutually rotated by 90° (see also Roy & Leweke 2008; Edstrand *et al.* 2016; Karami *et al.* 2019). Recognising the distinct symmetry of the integrals defined in (2.6*a*,*b*), we now use this expansion to express the kinematic meandering motion in terms of the leading POD modes $\phi_k(\boldsymbol{r})$. A similar approach was first applied by Bölle (2023) to the respective covariance operators, where also an estimate of the approximation error is derived.

From (2.7*b*), we see that only vorticity distributions that are symmetric in the Cartesian frame can have a contribution to the circulation, while any skew-symmetric vorticity patterns integrate to zero. Since the mean vorticity field is essentially axisymmetric (Bölle *et al.* 2023), to leading order,

$$\Gamma(t,z) = \int_V \mathrm{d}^2 r \left[\bar{w}^{eq}(\boldsymbol{r}) + \sum_{k=1}^{\infty} x_k(t,z)\,\phi_k(\boldsymbol{r})\right] \approx \int_V \mathrm{d}^2 r\, \bar{w}^{eq}(\boldsymbol{r}) = \text{const.} \tag{2.8}$$

Analogously, the vortex-centre integral (2.7*a*) is such that only skew-symmetric vorticity distributions can have a non-zero contribution. As recalled previously, we have considerable experimental evidence that the dominant vortex response modes are indeed skew-symmetric with the characteristic dipolar pattern shown in figure 1. We therefore obtain, to leading order ($i = 1, 2$),

$$r_{v,i}(t,z) = \frac{1}{\Gamma}\int_V \mathrm{d}^2 r\, r_i \left[\bar{w}^{eq}(\boldsymbol{r}) + \sum_{k=1}^{\infty} x_k(t,z)\,\phi_k(\boldsymbol{r})\right] \approx \left[\frac{1}{\Gamma}\int_V \mathrm{d}^2 r\, r_i\, \phi_i(\boldsymbol{r})\right] x_i(t,z). \tag{2.9}$$

Without loss of generality, we can take the coordinates r_i in (2.9) along the principal axes $\boldsymbol{e}_1, \boldsymbol{e}_2$, which are aligned with the leading dipolar vortex response modes (see figure 3 below). Due to orthogonality of the POD modes, $r_i\phi_k \sim \delta_{ik}$, $i, k = 1, 2$, and evaluating the last term in brackets in (2.9) gives a constant factor. This shows that $r_{v,i}(t,z) \sim x_i(t,z)$, $i = 1, 2$, i.e. the experimentally visible meandering motion (cf. figure 1) is proportional to an equivalent meandering motion in the phase space of the fluctuation dynamics.

In particular, meandering is, to leading order, confined to the two-dimensional manifold spanned by the leading two POD modes. We verified that this proportionality holds in the experiment (not shown); see also Bölle (2023, figure 3).

We emphasise that this derivation shows that vortex meandering is indeed associated with the variance-carrying modes (namely the leading POD modes). This was conjectured previously (e.g. Roy & Leweke 2008; Edstrand *et al.* 2016; Dghim *et al.* 2021) and already anticipated in § 2.1, but to the best of the authors' knowledge, has never been shown rigorously (part of the result has already been given in Bölle 2023). Thus, in what follows, we consider the bivariate spatiotemporal random process $x_i(t, z) = (w'(t, z), \phi_i)$ of principal components. A typical record in a fixed measurement plane at $z = \text{const.}$ is shown in figure 1.

2.4. *The universal vortex meandering characteristics*

Before introducing our theoretical meandering model in § 3, it is instructive to recall the principal meandering characteristics observed universally in experiments. Therewith, we pursue the twofold objective to (i) motivate our modelling strategy and (ii) lay down the minimum features that any candidate model must explain. For measurements taken in a fixed plane, these universal meandering characteristics are superposed on the smoke visualisation shown in figure 1 for the sake of illustration.

The identification of vortex meandering with a bivariate random process implies that a full characterisation would, in principle, require knowledge of all finite joint probability distributions (Yaglom 1962). In practice, we have considerable experimental evidence that the second-order correlation structure already encodes all essential aspects of the phenomenon. In particular, previous studies unanimously suggest the following.

(i) The empirical probability distribution of vortex meandering is close to Gaussian (e.g. Baker *et al.* 1974; Devenport *et al.* 1996; Bailey & Tavoularis 2008; Dghim *et al.* 2021).

(ii) The standard deviation of the vortex-centre position (referred to as meandering amplitude) increases monotonically downstream (e.g. Devenport *et al.* 1996; van Jaarsveld *et al.* 2011; Edstrand *et al.* 2016).

(iii) The associated leading-order vortex response corresponds to a dipolar fluctuation vorticity pattern approximately confined to the vortex core (e.g. Roy & Leweke 2008; Edstrand *et al.* 2016; Karami *et al.* 2019; Bölle *et al.* 2023).

(iv) The vortex response has a continuous power spectrum in each measurement plane, with variance levels monotonically increasing towards low frequencies (e.g. Devenport *et al.* 1996; Bailey & Tavoularis 2008; Bölle 2023). Equivalently, the estimated autocorrelation functions $\hat{\rho}_{ii}(\tau)$, shown in grey in figure 1, approximately follow an exponential autocorrelation function $\rho_{ii}(\tau) = \exp(-\lambda_i \tau)$, where λ_i denotes the reciprocal vortex response time.

While the importance of (some of) these features for the characterisation of vortex meandering was realised repeatedly (Baker *et al.* 1974; Devenport *et al.* 1996; Jacquin *et al.* 2001; van Jaarsveld *et al.* 2011; Edstrand *et al.* 2016), it seems that Bölle (2021) was the first to explicitly state that these characteristics are the typical signature of a Brownian motion (Chandrasekhar 1943; de Groot & Mazur 1984). To the best of the authors' knowledge, the first attempt at formulating a closed theory on this recognition is due to Bölle (2023).

3. Linear response theory of vortex meandering

In this section, we gradually introduce a linear stochastic model of vortex meandering. First, § 3.1 reviews the basic elements of a linear model approach. While this model still allows for very different mechanisms, we argue in § 3.2 that some can be precluded on experimental facts. On account of the phenomenology, we propose a conceptual meandering model in § 3.3, and derive characteristics that can be compared against experiments in § 3.4.

3.1. *Derivation of a linear model of vortex meandering*

Principally, the entire state of the system (vortex) is described by the generic dynamical variable $\boldsymbol{q}(t, z, \boldsymbol{r})$, for which the Reynolds decomposition $\boldsymbol{q}(t, z, \boldsymbol{r}) = \bar{\boldsymbol{q}}^{eq}(\boldsymbol{r}) + \boldsymbol{q}'(t, z, \boldsymbol{r})$ holds. As we are interested in only one particular aspect of the system dynamics (namely that associated with the meandering motion), we implicitly restrict to the pertinent submanifold of the dynamical variables. We then assume that, at least within this manifold, the dynamical variables obey a linear evolution equation of the form

$$\frac{\partial \boldsymbol{q}'}{\partial t} + U_\infty \frac{\partial \boldsymbol{q}'}{\partial z} = \boldsymbol{L}\boldsymbol{q}' + \boldsymbol{\xi}, \tag{3.1}$$

subject to initial and boundary conditions. In (3.1), $\boldsymbol{L} = \boldsymbol{L}[\bar{\boldsymbol{q}}^{eq}, \boldsymbol{\nabla}, R]$ denotes the symbolic linearised Navier–Stokes operator evaluated at the vortex mean state $\bar{\boldsymbol{q}}^{eq}$ and parametrised by the Reynolds number R. The forcing $\boldsymbol{\xi}$ represents the integral effect of the second-order nonlinear fluctuation dynamics, which is essentially localised in the free stream surrounding the vortex.

In our discussion so far, we have argued that the meandering dynamics corresponds to the spatiotemporal transport $(t, z) \mapsto x_i(t, z)$, which suggests the separation ansatz $\boldsymbol{q}'(t, z, \boldsymbol{r}) = a(t, z)\, \hat{\boldsymbol{q}}(\boldsymbol{r})$ of the corresponding dynamical variables. Then $x_i[\hat{\boldsymbol{q}}](t, z)$ is a function of the dynamical field $\hat{\boldsymbol{q}}(\boldsymbol{r})$ in the measurement plane.

Equation (3.1) corresponds to a description of the dynamics in a lab-fixed frame of reference. By the method of characteristics, we readily obtain the corresponding ordinary differential equation

$$\frac{\mathrm{d}\boldsymbol{q}'}{\mathrm{d}t} = \boldsymbol{L}\boldsymbol{q}' + \boldsymbol{\xi}, \quad \boldsymbol{q}'(0) = \boldsymbol{q}_0, \tag{3.2a,b}$$

where the initial condition is supposed to be a sure event (Chandrasekhar 1943; de Groot & Mazur 1984). Equations (3.2*a*,*b*) describe the vortex meandering dynamics as seen by a co-moving observer along the ray $z - U_\infty t = z_0$. This coordinate transform is corroborated by the finding that Taylor's hypothesis holds for vortex meandering perturbations (Jacquin *et al.* 2001).

Equations (3.2*a*,*b*) forms a vector-valued Cauchy problem. Its solution $t \mapsto \boldsymbol{q}'(t), \boldsymbol{q}'(t) \in L^2(M)$ for all t, traces a trajectory in the function space of spatial distributions of the dynamical variable in the measurement plane M released from the definite initial state $\boldsymbol{q}_0$. The space of square-integrable functions $L^2(M)$ is endowed with the inner product $(\boldsymbol{f}, \boldsymbol{g}) := \int_M \mathrm{d}^2 r \sum_i f_i(\boldsymbol{r})\, g_i^*(\boldsymbol{r})$, with induced norm $\|\boldsymbol{f}\| := \sqrt{(\boldsymbol{f}, \boldsymbol{f})}$.

Denoting by $\boldsymbol{L}^*$ the formal adjoint to $\boldsymbol{L}$ with respect to the inner product, the respective eigenvalue problems read

$$\boldsymbol{L}\boldsymbol{u}_i = \lambda_i \boldsymbol{u}_i \quad \text{and} \quad \boldsymbol{L}^* \boldsymbol{v}_i = \lambda_i^* \boldsymbol{v}_i, \tag{3.3a,b}$$

where bi-orthogonality $(\boldsymbol{v}_i, \boldsymbol{u}_j) = (\boldsymbol{v}_i, \boldsymbol{u}_i)\, \delta_{ij}$ holds. While principally we expect the eigenmodes to form a complete set to expand the linear vortex dynamics

(Fabre *et al.* 2006; Roy & Subramanian 2014), we assume that the meandering motion is represented by n relevant eigenmodes, in particular. Thus, we introduce the eigenvalue and eigenmode matrices $\Lambda_{ij} = \lambda_i \delta_{ij}$ and $\boldsymbol{U} = [\boldsymbol{u}_1, \boldsymbol{u}_2, \ldots, \boldsymbol{u}_n]$, $\boldsymbol{V} = [\boldsymbol{v}_1, \boldsymbol{v}_2, \ldots, \boldsymbol{v}_n]$. Using the eigenmode expansion $\boldsymbol{q}'(t) = \sum_{j=1}^{n} a_j(t)\, \boldsymbol{u}_j$ in (3.3*a*,*b*) yields

$$\frac{\mathrm{d}\boldsymbol{a}}{\mathrm{d}t} = \boldsymbol{\Lambda}\boldsymbol{a} + \boldsymbol{f}, \quad \boldsymbol{a}(0) = \boldsymbol{a}_0, \tag{3.4a,b}$$

upon projection onto the corresponding adjoint eigenmodes, where $f_j(t) := (\boldsymbol{v}_j, \boldsymbol{\xi}(t))$ and $a_{0,j} = (\boldsymbol{v}_j, \boldsymbol{q}_0)$. The general solution of (3.4*a*,*b*) reads

$$\boldsymbol{a}(t) - \mathrm{e}^{t\boldsymbol{\Lambda}}\, \boldsymbol{a}_0 = \mathrm{e}^{t\boldsymbol{\Lambda}} \int_0^t \mathrm{d}s\, \mathrm{e}^{-s\boldsymbol{\Lambda}} \boldsymbol{f}(s), \tag{3.5}$$

describing the dynamics in the manifold spanned by the n relevant eigenmodes. The corresponding evolution in physical space readily follows from expansion in the respective eigenmodes,

$$\boldsymbol{q}'(t) - \boldsymbol{U}\mathrm{e}^{t\boldsymbol{\Lambda}}\, \boldsymbol{a}_0 = \boldsymbol{U}\mathrm{e}^{t\boldsymbol{\Lambda}} \int_0^t \mathrm{d}s\, \mathrm{e}^{-s\boldsymbol{\Lambda}} \boldsymbol{f}(s). \tag{3.6}$$

Unlike this description of the dynamics in terms of eigenmodes, its characterisation in experiments is in terms of POD modes (see § 2). Alternative modal descriptions, e.g. by dynamic mode decomposition (Gutierrez-Castillo *et al.* 2022), are only recent to the best of the authors' knowledge. We notice that the combined analysis in terms of POD and eigenmodes is a common approach (de Groot & Mazur 1984). Projection of (3.6) onto the ith POD mode ϕ_i yields

$$(\boldsymbol{\phi}_i, \boldsymbol{q}'(t)) = \boldsymbol{\phi}_i^* \boldsymbol{U}\, \mathrm{e}^{t\boldsymbol{\Lambda}} \left[\boldsymbol{a}_0 + \int_0^t \mathrm{d}s\, \mathrm{e}^{-s\boldsymbol{\Lambda}} \boldsymbol{f}(s) \right] \tag{3.7}$$

$$\Longleftrightarrow \quad x_i(t) = \sum_{j=1}^{n} (\boldsymbol{\phi}_i, \boldsymbol{u}_j)\, \mathrm{e}^{t\lambda_j} \left[(\boldsymbol{v}_j, \boldsymbol{q}_0) + \int_0^t \mathrm{d}s\, \mathrm{e}^{-s\lambda_j}\, (\boldsymbol{v}_j, \boldsymbol{\xi}(s)) \right]. \tag{3.8}$$

Equation (3.8) identifies two general processes that contribute, in principle, to experimentally observed vortex meandering $x_i(t)$, namely (i) the amplification of initial perturbations and (ii) sustained forcing. Furthermore, since the eigenmodes $\boldsymbol{u}_j$ are not orthogonal, there will, in general, be several with non-null projection onto the ith POD mode. Thus, principally very different mechanisms may result in a practically identical, experimentally indistinguishable vortex response. Analyses of the different modal and non-modal growth mechanisms have been the subject of numerous previous studies (e.g. Antkowiak & Brancher 2004; Fabre *et al.* 2006; Fontane, Brancher & Fabre 2008; Hussain, Pradeep & Stout 2011; Mao & Sherwin 2012; Edstrand *et al.* 2016; Viola, Arratia & Gallaire 2016; Bölle *et al.* 2021; Qiu *et al.* 2021). The important point to be made here is that all these different approaches identify the same dipolar response pattern observed experimentally, yet by different physical mechanisms. Hence, which mechanism was operational in a particular experiment cannot be decided principally by solely inspecting the vortex response expanded in POD modes.

To the best of the authors' knowledge, which interaction pair $\{\boldsymbol{u}_i, \boldsymbol{v}_i\}$ is the most relevant in the experiment cannot be decided at present. Optimal forcing structures found in theory typically carry several orders of magnitude less energy than the associated response patterns, which makes their detection with standard tools focusing on variance-governing

modes (such as POD) difficult. Furthermore, they usually have a fine-grained, filament-like spatial structure that is not resolved in experiments, and even if it were, there is no reason to expect actually realised forcing to resemble the theoretical optimal. In fact, this is not even needed, since already a non-zero projection suffices. It is, however, possible to reject some mechanisms *a posteriori*, since the dynamical consequences are experimentally not observed.

At this point, it is convenient to pause our development of the meandering model to discuss the possible mechanisms. This will provide orientation about the next steps, as we can exclude some mechanisms on the basis of experimental evidence.

3.2. *Discussion of the candidate mechanisms*

In retrospect, it appears that previous attempts at explaining vortex meandering concentrated on only some of the universal characteristics identified in § 2.4. Early studies, emphasising the Gaussian distribution and broadband spectral signature, concluded that meandering is essentially the consequence of an 'inactive vortex being beaten by the surrounding turbulence' (e.g. Baker *et al.* 1974; Devenport *et al.* 1996), much like a 'passive tracer' (van Jaarsveld *et al.* 2011). On the other hand, already Bandyopadhyay *et al.* (1991) emphasised the 'dynamic nature' of the vortex, suggesting that meandering is not 'purely an artefact of the wind-tunnel environment' (Edstrand *et al.* 2016). Rather, it was suggested that meandering should be the consequence of an instability (e.g. Jacquin *et al.* 2001; Edstrand *et al.* 2016; Qiu *et al.* 2021). This shift in modelling paradigm was accompanied (or caused) by a change of the emphasised meandering characteristics to an exclusive consideration of the downstream amplitude growth and the dipolar vortex response pattern (cf. § 2.4).

The basic argument in favour of an instability mechanism is founded on the recognition that the leading POD mode pair, the fractional variance of which grows monotonically downstream, closely resembles eigenmodes found in stability analyses (Edstrand *et al.* 2016). Our above derivation (cf. (3.8)) implies that this conclusion cannot actually be drawn from the mere comparison of POD and eigenmodes. Even more, we are not aware of any vortex meandering experiment providing convincing evidence for the existence of an instability (Jacquin *et al.* 2001; Fabre & Jacquin 2004; Bailey & Tavoularis 2008; Edstrand *et al.* 2016; Bölle *et al.* 2023). This provides strong evidence that experimentally realised, isolated line vortices are in fact stable, and that we have to reject instability *sensu stricto* as the underlying mechanism.

Staying with the homogeneous solution in (3.8), it was conjectured that vortex meandering may be the consequence of transient growth (e.g. Fabre & Jacquin 2004; Roy & Leweke 2008; Mao & Sherwin 2012; Lee & Marcus 2024). Largely independent of the Reynolds number, Antkowiak & Brancher (2004) show that the time t_{opt} required to reach the optimal amplification by a transient-growth mechanism is of the order of ten rotation periods. That is, $t_{opt}/t_r \sim 10$, where $t_r := 2\pi\ell^2\Gamma_\infty^{-1}$ denotes the rotation time scale. Further defining the advection time scale $t_a := cU_\infty^{-1}$, we readily estimate $t_{opt}/t_a \sim 1$ with the estimated ratio $t_r/t_a \sim 10^{-1}$. This estimation suggests that transient growth operates over a downstream distance of the order of one chord length, contrary to the monotonic amplitude growth over downstream ranges of the order of at least ten chord lengths in experiments (Devenport *et al.* 1996; Bailey & Tavoularis 2008; van Jaarsveld *et al.* 2011; Bölle *et al.* 2023).

Eventually, we note that this estimation is consistent with the experiment of Bailey *et al.* (2018), who speculated that the vortex response may have contributions from transient

growth in their first measurement plane, albeit their experiment suggests that transient growth, even if it persisted afterwards, seemed overwhelmed by other mechanisms and was not clearly discernible for increased free-stream turbulence intensity. Therefore, while transient growth is likely not the governing mechanism of vortex meandering, the results nevertheless suggest that the underlying mechanism plays a role in experimental vortex dynamics.

We have considerable experimental evidence that changes in the intensity of the free-stream turbulence (e.g. grid turbulence) affect vortex meandering quantitatively rather than qualitatively (van Jaarsveld *et al.* 2011; Bailey *et al.* 2018). That is, enhanced free-stream turbulence intensities increase the meandering strength, but seem not to affect the principal characteristics. This suggests that meandering may be the result of some resonance mechanism, in which the vortex constitutes a self-stabilising entity that is continuously excited by the surrounding free-stream turbulence. The stabilising intrinsic vortex dynamics is associated with (Kelvin) waves propagating along the vortex core (Jacquin *et al.* 2001; Fabre & Jacquin 2004). In fact, very likely both aspects – sustained external forcing and intrinsic, stabilising vortex dynamics – are relevant (Bandyopadhyay *et al.* 1991; Fontane *et al.* 2008; Bailey *et al.* 2018).

Generally, the most important contribution to (3.8) will be from those perturbations that together maximise the different projections and are not too strongly damped. Theoretical studies indicate the existence of two near-neutral eigenmode families, referred to as D and L1 by Fabre *et al.* (2006), for which the vortex response pattern visually resembles the leading POD mode. While the displacement (D) waves are associated with an effectively normal linear operator, critical-layer (L1) waves are at the heart of the non-normal dynamics (Antkowiak & Brancher 2004; Fontane *et al.* 2008; Bölle *et al.* 2021). On account of our discussion, we assume that vortex meandering is essentially governed by a critical-layer dynamics. Thence, supposing a single governing mode j, introducing the shorthand identifications $x_{0,i} \leftarrow (\phi_i, \boldsymbol{u}_j)(\boldsymbol{v}_j, \boldsymbol{q}_0)$ and $f_i(t) \leftarrow (\phi_i, \boldsymbol{u}_j)(\boldsymbol{v}_j, \boldsymbol{f}(t))$, (3.8) simplifies to

$$x_i(t) - \mathrm{e}^{t\lambda_i} x_{0,i} = \mathrm{e}^{t\lambda_i} \int_0^t \mathrm{d}s\, \mathrm{e}^{-s\lambda_i} f_i(s) \quad (i = 1, 2), \tag{3.9}$$

where we have used the experimental evidence that meandering is associated with the leading two POD modes (§ 2.3).

From the stability analysis of Fabre *et al.* (2006), we estimate that a characteristic vortex response time scale $t_s = \lambda_i^{-1}$ should to be of the order of $t_s/t_r \sim 10^2$. With our above scale estimates, we readily obtain $t_s/t_a \sim 10$, in agreement with our previous conclusions.

3.3. *Phenomenology and conceptual vortex meandering model*

In order to frame vortex meandering in the concepts of statistical mechanics, we start from an abstraction of the general experimental set-up outlined in § 2.1. To a first approximation, we may consider the experimental configuration as consisting of an isolated vortex evolving in a (weakly) turbulent free stream. In the language of statistical mechanics, we identify the vortex with our system, and refer to the free-stream turbulence as a heat bath. The intensity of the heat bath will be given by the free-stream turbulence intensity u of the empty facility.

As a qualitative model of the heat bath, we may imagine the free-stream turbulence filling the wind tunnel to be an assembly of a very large number of small-scale vortices, evolving rapidly over a very short time scale t_f. We therefore assume that the free-stream turbulence has no particular spatial or temporal structure, thus being characterised by

stationary and homogeneous statistics. Putting the large-scale vortex in the heat bath, we think of the small-scale vortices exerting minute excitations in very rapid succession. While we do not know the details of each elementary excitation, slow (scale t_s) reactions of the large-scale vortex integrate over time. This essentially corresponds to a Brownian motion – where each elementary excitation is highly complicated and unobserved, the integral effect of very many minute events accumulates to a macroscopic and visible effect, manifest in figure 1.

On account of this phenomenology, we assume that the time scale separation $t_s \gg t_f$ holds between the characteristic scales of the large-scale vortex and the surrounding small-scale turbulence. Then on the slow time scale t_s, the forcing approximately corresponds to a white noise process, with

$$\bar{f}_i^{\boldsymbol{x}_0}(t) = 0, \quad \overline{f_i(s) f_j(t)}^{\boldsymbol{x}_0} = 2B_{ij}\,\delta(t-s) \quad (i,j=1,2), \tag{3.10a,b}$$

where B_{ij} determines the strength and mutual correlation of the forcing. With this additional assumption on the forcing statistics, (3.4*a*,*b*) corresponds to a Langevin equation, while its solution (3.5) (or (3.9)) is known as an Ornstein–Uhlenbeck process, describing a Brownian motion (Chandrasekhar 1943; Yaglom 1962; de Groot & Mazur 1984). We emphasise that consequently, framing vortex meandering as a problem in stochastic mechanics contains both previous explanation families (cf. § 1) as limiting cases. Linear deterministic dynamics results as the external fluctuations asymptotically tend to zero, while a purely externally driven dynamics would be the consequence of a vanishing intrinsic vortex resistance.

3.4. *Non-equilibrium dynamics of the Langevin system*

Equations (3.9)–(3.10) summarise our final vortex meandering model, taking the form of a Langevin equation. In the following, we derive characteristic model properties that can be evaluated statistically in experiments. The relevant methodology for this purpose will be introduced in § 4.

3.4.1. *Gaussian probability distribution*

Our assumption of time scale separation implies the existence of an intermediate time increment Δt such that $t_f \ll \Delta t \ll t_s$. We can then expand the particular solution as

$$\begin{aligned}\boldsymbol{x}(t) - \mathrm{e}^{t\boldsymbol{\Lambda}}\boldsymbol{x}_0 = \mathrm{e}^{t\boldsymbol{\Lambda}}\int_0^t \mathrm{d}s\,\mathrm{e}^{-s\boldsymbol{\Lambda}}\boldsymbol{f}(s) = \mathrm{e}^{t\boldsymbol{\Lambda}}\sum_{k=0}^{K-1}\int_{k\,\Delta t}^{(k+1)\,\Delta t}\mathrm{d}s\,\mathrm{e}^{-s\boldsymbol{\Lambda}}\boldsymbol{f}(s)\\ \approx \sum_{k=0}^{K-1}\mathrm{e}^{(t-k\,\Delta t)\boldsymbol{\Lambda}}\int_{k\,\Delta t}^{(k+1)\,\Delta t}\mathrm{d}s\boldsymbol{f}(s) = \sum_{k=0}^{K-1}\mathrm{e}^{(t-k\,\Delta t)\boldsymbol{\Lambda}}\boldsymbol{W}(\Delta t).\end{aligned} \tag{3.11}$$

Here, we have used that due to time scale separation, the exponential function is practically constant over the time increment. Formally, (3.11) expresses meandering as a random walk, where each 'step' $\boldsymbol{W}(\Delta t)$ of the vortex is the integral over a succession of a great many minute excitations, $\int_{k\,\Delta t}^{(k+1)\,\Delta t}\mathrm{d}s\,\boldsymbol{f}(s)$. Thus, the slow vortex fluctuation dynamics is the sum over a large number $K \gg 1$ of independent, identically distributed excitation events. By the central limit theorem, we therefore conclude that the vortex dynamics must have a Gaussian distribution (Chandrasekhar 1943, Lemma I on p. 23).

3.4.2. *Two-point statistics in evolution time*

If meandering corresponds to a Markov process, we further need to specify the correlation structure to obtain a complete classification of the stochastic dynamics.

Taking the mean of (3.9) for a trajectory started from a definite initial perturbation yields

$$\bar{\boldsymbol{x}}^{\boldsymbol{x}_0}(t) = \mathrm{e}^{t\boldsymbol{\Lambda}}\,\boldsymbol{x}_0 \tag{3.12}$$

on account of the forcing statistics (3.10). Equation (3.12) is formally identical to the homogeneous solution of the associated deterministic problem, and as such, subject to the linear-stability and transient-growth studies discussed in § 3.2. That is, in a systematically stochastic theory, practically deterministic dynamics is an approximation valid in the limit of a sharp transition probability density $f(\boldsymbol{x}_0 \,|\, \boldsymbol{x}, t)$ (de Groot & Mazur 1984).

The leading-order variability around the mean trajectory (3.12) is given by the covariance

$$\boldsymbol{C}(t) = \overline{(\boldsymbol{x}-\bar{\boldsymbol{x}}^{\boldsymbol{x}_0})(\boldsymbol{x}-\bar{\boldsymbol{x}}^{\boldsymbol{x}_0})^*}^{\boldsymbol{x}_0}(t) = 2\int_0^t \mathrm{d}s\,\mathrm{e}^{(t-s)\boldsymbol{\Lambda}}\,\boldsymbol{B}\,\mathrm{e}^{(t-s)\boldsymbol{\Lambda}^*}. \tag{3.13}$$

Further, let $\boldsymbol{C}^{eq}$ be the covariance associated with the equilibrium probability distribution. Then the competition between sustained stochastic excitation by the surrounding free stream and the intrinsically stabilising vortex dynamics (cf. § 3.2) implies asymptotic convergence, $\boldsymbol{C}^{eq} = \boldsymbol{C}(t\to\infty)$. The fluctuation–dissipation theorem (de Groot & Mazur 1984)

$$\boldsymbol{\Lambda}\boldsymbol{C}^{eq} + \boldsymbol{C}^{eq}\boldsymbol{\Lambda}^* = 2\boldsymbol{B} \tag{3.14}$$

uniquely relates the equilibrium covariance of the vortex response to the intensity of the exciting turbulence. A POD of the fluctuation–dissipation theorem (3.14) is the subject of stochastic forcing analyses (Farrell & Ioannou 1996; Fontane *et al.* 2008).

For the particular case of modal dynamics (3.9), the components of (3.13) uncouple and we obtain the variance evolution

$$\sigma_i^2(t) = \overline{(x_i-\bar{x}_i^{\boldsymbol{x}_0})^2}^{\boldsymbol{x}_0}(t) \sim \mathcal{U}^2\left(1-\mathrm{e}^{2\lambda_i t}\right) \quad (i=1,2) \tag{3.15}$$

upon setting $B_{ij}\sim\mathcal{U}^2\,\delta_{ij}$ (Bölle 2023). For t of the order of the vortex response time $t_s = \lambda_i^{-1}$, we approximate (3.15) by its leading-order expansion (Bölle 2023)

$$\sigma_i^2(t) \sim 2\mathcal{U}^2\lambda_i t \sim 2\mathcal{U}^2\,\frac{t}{t_s}. \tag{3.16}$$

This law of variance growth was proposed on phenomenological reasoning by van Jaarsveld *et al.* (2011), and found to hold for other experiments (Bailey *et al.* 2018; Bölle 2021, 2023).

3.4.3. *Two-point statistics in measurement time*

By design, we expect experiments to have reached stationarity when performing measurements (cf. § 5.3). Measurement sequences in fixed planes (at $z=\text{const.}$) are then amenable to Fourier analysis. For the Langevin model (3.9)–(3.10), the equilibrium autocovariance function and power spectrum read (Yaglom 1962; von Storch & Zwiers 2003)

$$C_{ii}(\tau) = \sigma_i^2\,\mathrm{e}^{-\lambda_i|\tau|} \quad\text{and}\quad G_{ii}(\omega) = \frac{\sigma_i^2\lambda_i}{\pi}\,\frac{1}{\lambda_i^2+\omega_i^2} \quad (i=1,2). \tag{3.17}$$

We recall that our Brownian motion vortex meandering model is essentially parametrised by two variables, $\mathcal{U}$ and t_s, measuring the strength of the surrounding

turbulence and the vortex response time scale, respectively. This is in agreement with the findings of van Jaarsveld *et al.* (2011) and Bailey *et al.* (2018), who assumed that t_s was given by the vortex rotation time scale t_r. In § 3.1, we show that t_s is related to the eigenvalues of the linearised vortex dynamics, and more specifically, argue in § 3.2 that vortex meandering may likely be associated with critical-layer vortex waves. Hence, in principle, t_s can be determined if the vortex mean flow and the external flow parameters (e.g. Reynolds number) are known. We have considerable experimental evidence that vortex meandering is directly proportional to the intensity of the surrounding turbulence but not affected by its spectral signature (Bailey & Tavoularis 2008; van Jaarsveld *et al.* 2011; Bailey *et al.* 2018; Dghim *et al.* 2021). This is reflected in the model proposed here. Thus, the formulae of this section could in principle also be used to predict vortex meandering, provided that the vortex mean flow, the Reynolds number and the turbulence intensity are known. These predictions should capture the right qualitative behaviour; however, a quantitatively correct prediction of the meandering motion would require scaling terms of order unity omitted here (cf. §§ 3.1–3.2 and Bölle 2023).

4. Statistical inference: relating theory and experiment

So far in this study, we have disposed of two descriptive elements for the phenomenon of vortex meandering, namely (i) the mathematical model introduced in § 3, and (ii) an experiment relative to the phenomenon in question (cf. § 2). While at the outset these two elements pertain to entirely different spheres (Cramér 1963), we derived model characteristics in § 3.4 that can be estimated in experiments. Statistical inference provides the theoretical frame and tools to assess given statistical data in the context of the adopted model. This, principally, gives us the possibility of confirming or rejecting our model on an objective and reproducible statistical basis.

4.1. *Sampling*

For the purpose of this study, we formally identify the wind tunnel experiment with a random experiment $\mathfrak{E}$. One realisation of $\mathfrak{E}$ corresponds to a spatial meandering trajectory $z \mapsto X^{(t)}(z)$, drawn at random from the totality of all admissible meandering paths (called the population). In this sense, the snapshot shown in figure 1 for some time instant t represents one such realisation of $\mathfrak{E}$. Keeping the experimental conditions fixed and running the wind tunnel experiment over a certain time T, while recording the outcomes at the rate Δt, corresponds conceptually to the repetition of $\mathfrak{E}$ $N = T/\Delta t$ times. The result of one measurement run will be a sequence of particular realisations, all drawn at random from the same probability distribution. This subset of the entire population is called the sample (Cramér 1963). Current experiments do not resolve the downstream meandering trajectory; rather, only samples gathered in a small number of measurement planes at fixed z (cf. § 2.1) are experimentally available. Thus, while principally $\mathfrak{E}$ corresponds to a function-valued random process, our further analysis is limited to scalar-valued samples. Let us formalise these notions.

Consider a random experiment $\mathfrak{E}$ connected with a random variable X taking values from some parent population, $\mathbb{R}$ say, according to the distribution function $F_X(x)$. Suppose that we repeat $\mathfrak{E}$ N times; then the outcome of the nth trial is the actual realisation $X^{(n)} = x_n$, where $n = 1, 2, \ldots, N$. The set of realisations $\boldsymbol{x}_N^{(k)} = \{x_1^{(k)}, x_2^{(k)}, \ldots, x_N^{(k)}\} \subset \mathbb{R}$ is called a random sample. Of course, we could, in theory, repeat the sampling process, i.e. drawing N times anew from $\mathfrak{E}$, which leads to another equally possible random sample

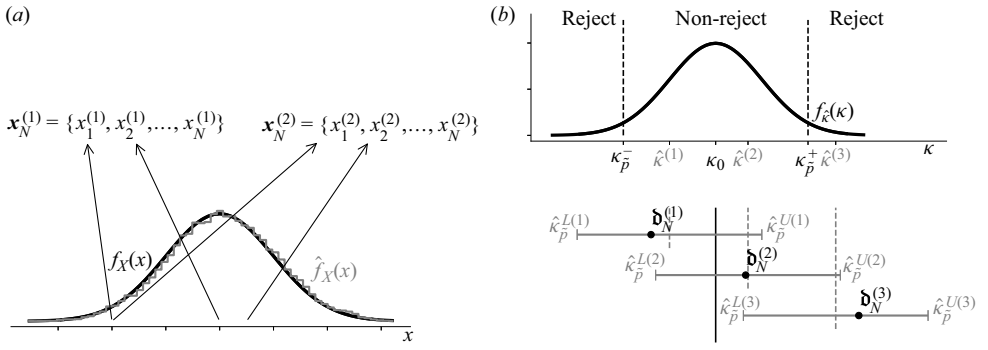

Figure 2. Basic elements of the theory of estimation and hypothesis testing. (*a*) Schematic of the sampling process for the random variable X having probability density $f_X(x)$ (empirical density $\hat{f}_X(x)$). Repetition of the sampling yields *a priori* different samples $\boldsymbol{x}_N^{(k)}$ of the population. (*b*) The kth point estimator $\hat{\kappa}^{(k)}$ and confidence interval $(\hat{\kappa}_{\tilde{p}}^L, \hat{\kappa}_{\tilde{p}}^U)^{(k)}$ of the statistical characteristic κ with true population value κ_0. The sampling distribution (density $f_{\hat{\kappa}}(\kappa)$) determines the variability of the estimator and interval width. The non-rejection region $\Theta(\tilde{p}) = (\kappa_{\tilde{p}}^-, \kappa_{\tilde{p}}^+)$ of the null hypothesis $H_0 : \kappa = \kappa_0$ at the $(1 - \tilde{p}) \times 100\,\%$ significance level is indicated. Schematic test statistics $\mathfrak{d}_N^{(k)}$ for different samples illustrate the duality with the confidence intervals.

(von Storch & Zwiers 2003). To emphasise the random nature of the sample, we denote the kth realisation by $\boldsymbol{x}_N^{(k)}$. The process of sampling is shown schematically in figure 2(*a*).

4.2. *Theory of estimation and hypothesis testing*

4.2.1. *Estimation*

Typically, random variables are characterised in terms of statistical characteristics κ (e.g. expectation and variance) taking fixed non-random values κ_0, say. On the other hand, the corresponding sample characteristics (e.g. sample mean and variance) are computed by (nonlinearly) combining the random sample elements $x_n^{(k)}$, $n = 1, 2, \ldots, N$. Therefore, unlike the non-random population characteristics, sample characteristics are again random variables. To discriminate between population and sample characteristics, we adopt the usual convention to denote the kth estimator of the true characteristic $\kappa = \kappa_0$, computed from the kth sample $\boldsymbol{x}_N^{(k)}$, by $\hat{\kappa}_N^{(k)} = \hat{\kappa}(\boldsymbol{x}_N^{(k)})$.

Since $\hat{\kappa}_N$ is a random variable, a full characterisation requires knowledge of its probability distribution. This sampling distribution $F_{\hat{\kappa}}(\kappa)$ is specific to each sample characteristic $\hat{\kappa}_N$, and uniquely determined by the distribution function $F_X(x)$ (Cramér 1963). In particular, the sampling distribution determines the variability of the associated sample characteristic. This is displayed schematically in figure 2(*b*), showing the sampling probability density $f_{\hat{\kappa}}(\kappa)$ of some arbitrary characteristic along with possible estimates $\hat{\kappa}_N^{(k)}$ computed from three different samples $\boldsymbol{x}_N^{(k)}$, $k = 1, 2, 3$. This example illustrates that point estimators $\hat{\kappa}_N^{(k)}$ will generally be different for each sample and different from the true characteristic κ_0.

We emphasise that the above definition of a sample characteristic as a function of the sample, in principle, allows for an infinite number of candidate estimators. Each estimator is fully determined by its unique sampling distribution, the statistical characteristics of which define the estimator properties and usefulness. In practice, the assessment of the quality of any given estimator is essentially based on the expectation and variance of the estimator. An estimator is called unbiased if its expectation equals the population

characteristic, i.e. $E(\hat{\kappa}_N) = \kappa_0$ for all N. It is further desirable that estimators are in an as close neighbourhood of the true value as possible. This leads to a definition of the efficiency of an estimator $E((\hat{\kappa}_N - \kappa_0)^2) = (E(\hat{\kappa}_N) - \kappa_0)^2 + V(\hat{\kappa}_N)$ as the sum of its squared bias and variance. The objective is to find unbiased and minimum-variance estimators. A systematic approach to obtain estimators is by the maximum likelihood method (Cramér 1963; von Storch & Zwiers 2003).

Our discussion so far makes clear that point estimators are random functions that map given samples on random values. As such, one particular value of the characteristic $\hat{\kappa}_N^{(k)}$, realised in the experiment $\boldsymbol{x}_N^{(k)}$, is of limited significance. Rather, reliable statements require robust estimates of the characteristic that, although obtained from only one sample, have value for all experiments that could have been conducted alternatively. This is the purpose of interval estimators (von Storch & Zwiers 2003). The confidence interval indicates the uncertainty in the estimate that is unavoidable since we are working with a finite sample of the total population. If we were to draw samples again and again *ad infinitum*, then the confidence intervals would cover the non-random population characteristic κ_0 with a certain *a priori* percentage $\tilde{p}$. In other words, the confidence interval is obtained for the specific sample, and the confidence level $\tilde{p}$ indicates its validity for the totality of all samples that could have been obtained alternatively. We see that as with point estimators, confidence intervals (having random endpoints) are again random functions of the sample. This is shown schematically in the lower part of figure 2(*b*).

4.2.2. *Hypothesis testing*

Given a set of measurements, namely a sample, we would like to decide if it is consistent with some theoretical model defined *a priori*. In order to approve or reject agreement, we define representative characteristics κ that we know to take the value κ_0 in the model, and suppose this to be true. That is, we conjecture the null hypothesis $H_0 : \kappa = \kappa_0$. We then estimate κ by the corresponding sample characteristic $\hat{\kappa}_N$, and compare the result with the postulated true value. Our previous discussion implies that, in general, equality will never hold exactly, even if H_0 is true, and since $\hat{\kappa}_N$ is a random variable, the agreement will be different for each sample that we test for. We therefore have to specify difference thresholds beyond which we reject the model, because the difference between $\hat{\kappa}$ and κ_0 is very unlikely to be due to random variability. This suggests the following practical implementation, the essential elements being shown schematically in figure 2(*b*).

Define a test statistic $\mathfrak{d}_N = \mathfrak{d}(\boldsymbol{x}_N)$ in the form of a distance measure $\mathfrak{d}(\boldsymbol{x}_N) = \mathrm{dist}(\hat{\kappa}_N, \kappa_0)$. This will, in general, be a nonlinear function of the sample $\boldsymbol{x}_N$, therefore the test statistic is itself a random variable with a specific sampling distribution. Fix a non-rejection region, i.e. an interval $\Theta(\tilde{p}) = (\kappa_{\tilde{p}}^-, \kappa_{\tilde{p}}^+)$ (around the hypothesised true value κ_0) containing $\tilde{p} \times 100\,\%$ of the realisations of $\mathfrak{d}(\boldsymbol{x}_N)$ when H_0 is true. The interval is determined by the sampling distribution of the test statistic $\mathfrak{d}_N$ (Wilks 2006). The risk $(1 - \tilde{p}) \times 100\,\%$ of falsely rejecting the true null hypothesis is called the significance level, usually set to 5 %–10 % (von Storch & Zwiers 2003). If the actual realisation of the test statistic $\mathfrak{d}(\boldsymbol{x}_N)$ falls outside the interval $\Theta(\tilde{p})$, then H_0 is rejected at the $(1 - \tilde{p}) \times 100\,\%$ significance level (Cramér 1963; von Storch & Zwiers 2003; Bendat & Piersol 2010).

4.3. *The equivalent sample size*

In mathematical statistics, sampling means drawing a collection of independent and identically distributed random variables, yielding a set of realisations. Often, in practice,

sampling means discretely recording data from a time series. In general, the elements of samples obtained in this way will be correlated, hence the independence assumption fails. In order to be able to use the theoretical results, we assume the sample to be drawn from a stationary, ergodic process (von Storch & Zwiers 2003).

Usually encountered time series have finite correlation (Yaglom 1962), suggesting that the full sample contains subsets of independent observations (Tennekes & Lumley 1972). Sub-sampling, i.e. considering only sample elements separated by some multiple of the correlation length, therefore would seem to be a simple and straightforward approach to obtain an independent sample from serially correlated data. However, it is known that by this approach, information is lost without improving the estimate (von Storch & Zwiers 2003). Thus, rather than throwing away 'intermediate' observations between any two independent elements, we use the full sample and introduce an equivalent sample size based on the autocorrelation structure of the time series (Leith 1973; Trenberth 1984; Thiébaux & Zwiers 1984; Zwiers & Von Storch 1995).

The equivalent sample size is defined as the number of independent random variables needed to provide the same amount of information about the population characteristic as contained in the full sample of dependent variables. As such, the equivalent sample size depends on the characteristic to be tested and how information is measured (Trenberth 1984; von Storch & Zwiers 2003; Wilks 2006). Letting κ be this characteristic, the number of independent elements in a sample (relative to κ) is defined as

$$N'(\kappa) := \frac{T}{2\,t_I(\kappa)} = \frac{N}{2\,\dfrac{t_I(\kappa)}{\Delta t}}, \quad T = N\,\Delta t. \tag{4.1}$$

Here, T denotes the total measurement time of the time series, equal to $N\,\Delta t$ if the N sample elements are recorded at the constant time step Δt (cf. § 2.1), and $t_I(\kappa)$ is the integral time scale relative to κ. As usual, we refer to twice the integral time scale as the decorrelation time, and write $t_D = 2t_I$ (Leith 1973; Trenberth 1984; von Storch & Zwiers 2003).

The decorrelation time for the mean can be estimated in a finite, discrete sample of length N by (Thiébaux & Zwiers 1984; von Storch & Zwiers 2003)

$$t_D \approx \left[1 + 2\sum_{\nu=1}^{N-1}\left(1 - \frac{\nu}{N}\right)\rho(\nu)\right]\Delta t \approx \left[1 + 2\sum_{\nu=1}^{N-1}\rho(\nu)\right]\Delta t, \tag{4.2}$$

where we assume that $T \gg t_I$ and that the autocorrelation $\rho(\nu)$ decays to zero sufficiently fast as the lag $\nu = \tau/\Delta t \to \infty$, $\Delta t \neq 0$ (Tennekes & Lumley 1972). Analogously, estimates of the decorrelation time are obtained for other characteristics; in particular,

$$t_D \approx \left[1 + 2\sum_{\nu=1}^{N-1}\rho^2(\nu)\right]\Delta t \quad \text{for the variance,} \tag{4.3}$$

$$t_D \approx \left[1 + 2\sum_{\nu=1}^{N-1}\rho_X(\nu)\rho_Y(\nu)\right]\Delta t \quad \text{for the correlation} \tag{4.4}$$

(see also Bartlett 1935; Bayley & Hammersley 1946; Trenberth 1984; von Storch & Zwiers 2003). From (4.2)–(4.4), we see immediately that $t_D \to \Delta t$ as $\rho(\nu) \to 0$, thus $N' \to N$ by (4.1*a*,*b*). That is, if it happens that the time series is uncorrelated (i.e. white noise), then the

equivalent sample size degenerates to the full sample size. If the time series comes from a first-order autoregressive process, then all the decorrelation – or equivalently, persistence information – is contained in the lag-1 correlation $\rho_1 := \rho(\nu = \Delta t) = \exp(-\Delta t/t_I)$ (Wilks 2006), which can be used to derive simplified estimates for the decorrelation times.

Eventually, we note that the autocorrelation functions $\rho(\nu)$ in (4.2)–(4.4) are not known *a priori* in general, and have to be estimated; that is, we take $\hat{\rho}(\nu)$ in (4.2)–(4.4), in practice. It is known that estimates of N' that are computed directly from the estimators of the autocorrelation or power spectrum perform poorly (Thiébaux & Zwiers 1984). Rather, the best option is to estimate N' from a fit to an autoregressive-model (Thiébaux & Zwiers 1984; Trenberth 1984; von Storch & Zwiers 2003).

5. Results and discussion

In this section, we use the statistical inference tools introduced in § 4 to provide evidence that the given experiment of § 2 is consistent with the theoretical model proposed in § 3. We provide quantitative measures of this agreement that are significant and transferable at precisely given levels. In particular, we show that experimentally observed vortex meandering is conveniently described by a stationary, ergodic Gauss–Markov process.

5.1. *Proper orthogonal decomposition*

Suppose that the streamwise component of the fluctuation vorticity field in the measurement plane M is a vector-valued random process $t \mapsto w'(t, \boldsymbol{r})$ such that $w'(t) \in L^2(M)$ for all t. This distinction between temporal and spatial coordinates suggests the separation ansatz

$$w'(t, \boldsymbol{r}) = \sum_{i=1}^{\infty} x_i(t)\, \phi_i(\boldsymbol{r}), \quad x_i(t) = (\phi_i, w'(t)), \tag{5.1a,b}$$

where $(\cdot, \cdot)$ denotes the L^2-inner product (§ 3.1). From the above, (5.1*a*,*b*) corresponds to an expansion of the fluctuation vorticity in terms of deterministic spatial modes $\phi_i \in L^2(M)$ superposed at random according to the time series of random expansion coefficients $x_i(t)$.

While principally any set of spatial modes ϕ_i that spans $L^2(M)$ can be used in (5.1*a*,*b*), the fact that vortex meandering is associated with the energy-carrying, slow scales of the vortex fluctuation dynamics can be used to reduce the degrees of freedom considerably. The POD relies on those modes maximising the variance content in a truncated expansion (Holmes *et al.* 1996), hence a restriction to the variance-carrying scales is realised optimally by working in the linear manifold spanned by the leading d POD modes. The optimality condition of POD translates into the eigenvalue problem

$$C\phi_i = \sigma_i^2 \phi_i, \tag{5.2}$$

where C denotes the vorticity covariance integral operator. Following standard terminology, we refer to ϕ_i as the ith POD mode, and the associated expansion coefficient $x_i(t)$ as the ith principal component time series. It is always possible to order the eigenvalues in the non-increasing, non-negative sequence $\sigma_1^2 \geq \sigma_2^2 \geq \cdots \geq 0$. In this way, the associated POD modes are ranked in terms of their contribution σ_i^2 to the total vorticity variance contained in M.

For practically finite samples, we have to estimate the covariance operator in (5.2). The maximum likelihood estimator reads (von Storch & Zwiers 2003)

$$\hat{\boldsymbol{C}} = \frac{1}{N}\sum_{n=1}^{N}(\boldsymbol{w}_n - \bar{\boldsymbol{w}})(\boldsymbol{w}_n - \bar{\boldsymbol{w}})^*, \tag{5.3}$$

where $\boldsymbol{w}_n \in \mathbb{R}^P$, $n = 1, 2, \ldots, N$, are the spatially discrete vorticity measurements, $\bar{\boldsymbol{w}}$ is their sample mean (see § 5.2), and an asterisk denotes the matrix transpose. Solving the eigenvalue problem (5.2) with an estimated covariance operator (5.3) yields only estimates $\hat{\boldsymbol{\phi}}_i \in \mathbb{R}^P$ and $\hat{\sigma}_i^2$. In order to assess the uncertainty in the ith estimate, North *et al.* (1982) propose

$$\Delta\sigma_i^2 \approx \sigma_i^2\sqrt{\frac{2}{N'}} \quad \text{and} \quad \Delta\boldsymbol{\phi}_i \approx \frac{\Delta\sigma_i^2}{\sigma_i^2 - \sigma_j^2}\boldsymbol{\phi}_j \tag{5.4a,b}$$

as a 'rule of thumb', where σ_j^2 denotes the eigenvalue closest to σ_i^2. Since the eigenvalues can be arranged in a non-increasing sequence, the modal uncertainty is non-negative, with $\Delta\sigma_i^2/(\sigma_i^2 - \sigma_j^2) \to \infty$ as $\sigma_j^2 \to \sigma_i^2$, i.e. as the ith eigenvalue degenerates. In this case, the corresponding eigenmodes span an eigenspace having the dimension of the degeneracy. Consequently, the individual eigenmodes are completely undetermined as long as together they span the eigenspace. Hence, we refer to $\Delta\sigma_i^2/(\sigma_i^2 - \sigma_j^2)$ as the indiscernibility factor measuring the modal uncertainty due to eigenvalue degeneracy. Of course, as the POD eigenvalues are not known *a priori*, we have to use the estimates $\hat{\sigma}_i^2$ in place of σ_i^2.

In order to account for serial correlation in the data, we use the equivalent sample size N' in (5.4*a*,*b*). However, unlike Hannachi, Jolliffe & Stephenson (2007), who use the decorrelation time for the mean (4.2), the proper choice would be to compute N' with t_D for the variance (4.3), as also emphasised by Wilks (2006).

Contour plots of the leading POD mode pair are shown in figure 3 together with the respective uncertainties according to (5.4*a*,*b*). Figure 4(*b*) further displays the indiscernibility factors for the first ten POD modes, showing that the uncertainty in the leading pair is $O(10^{-1})$. The dashed line indicates the threshold for which $\Delta\sigma_i^2 = (\sigma_i^2 - \sigma_j^2)$, that is, the difference between neighbouring eigenvalues equals their uncertainty. Thus, POD modes are mutually discernible only below the dashed line, while all modes above are practically indiscernible. Figure 4(*a*) shows the estimated eigenvalue spectrum together with the respective uncertainties (5.4*a*,*b*). In particular, we see that the leading POD mode pair of interest here is not degenerate.

Henceforth, confining to the manifold spanned by the leading POD mode pair (figure 3), the meandering dynamics corresponds to the principal component time series $x_i(t)$, $i = 1, 2$.

5.2. *Sample variance in the vortex meandering manifold*

Given the definition of the expectation and variance, we define the corresponding sample mean and sample variance by replacing $F(x)$ with the empirical distribution $\hat{F}(x)$ in (2.3*a*,*b*):

$$\hat{\mu} = \int_{-\infty}^{+\infty} x\,\mathrm{d}\hat{F}(x) = \frac{1}{N}\sum_{n=1}^{N} x_n \tag{5.5}$$

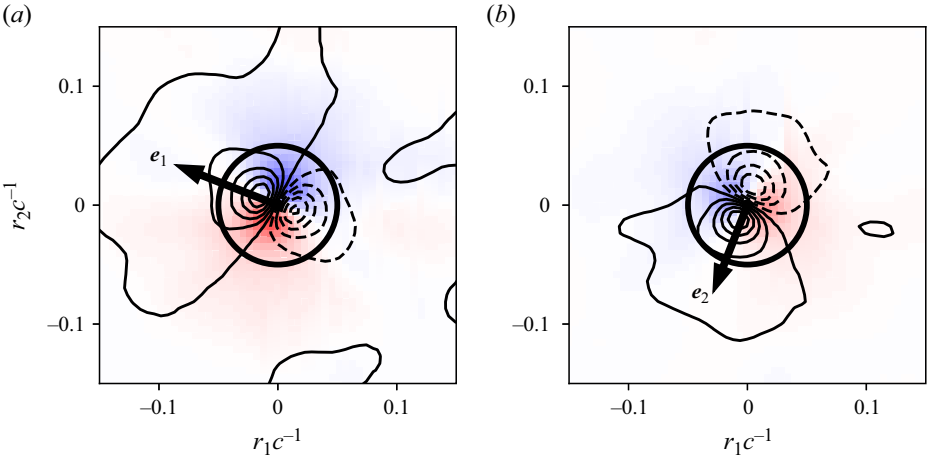

Figure 3. Estimate and uncertainty of the leading POD modes in the last measurement plane: (*a*) first mode $\hat{\phi}_1(\boldsymbol{r})$, (*b*) second mode $\hat{\phi}_2(\boldsymbol{r})$. Contours display POD mode estimates with solid (dashed) contours indicating positive (negative) values. Uncertainties from the North *et al.* (1982) rule of thumb (5.4*a*,*b*) are shown as colour shading, with red (blue) indicating positive (negative) values. The circle delimits the vortex core (radius $r_c c^{-1} = 5 \times 10^{-2}$), and the principal vectors of the vortex-centre time series are shown as arrows.

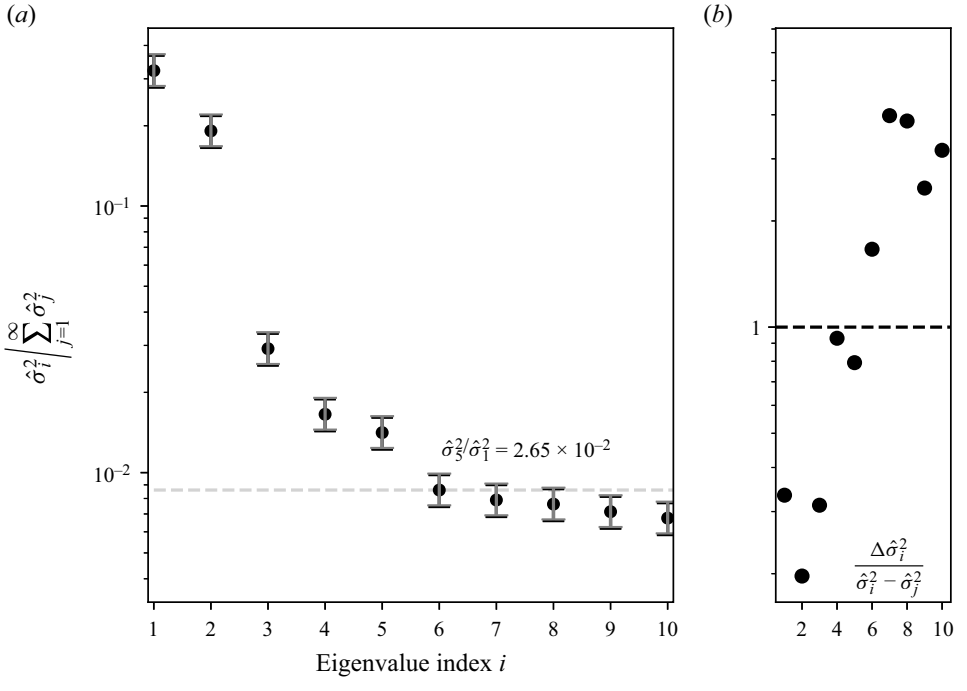

Figure 4. The POD eigenvalue spectrum in the last measurement plane. (*a*) Estimates of the eigenvalues (black dots) and the respective 95 % confidence intervals computed according to the North *et al.* (1982) rule of thumb (black). Practically identical confidence intervals (grey) are obtained from the $\chi^2(N' - 1)$ distribution of the sample variance. (*b*) Indiscernibility factor, measuring POD mode uncertainty, with a value of unity indicating the threshold beyond which modes are mutually indiscernible.

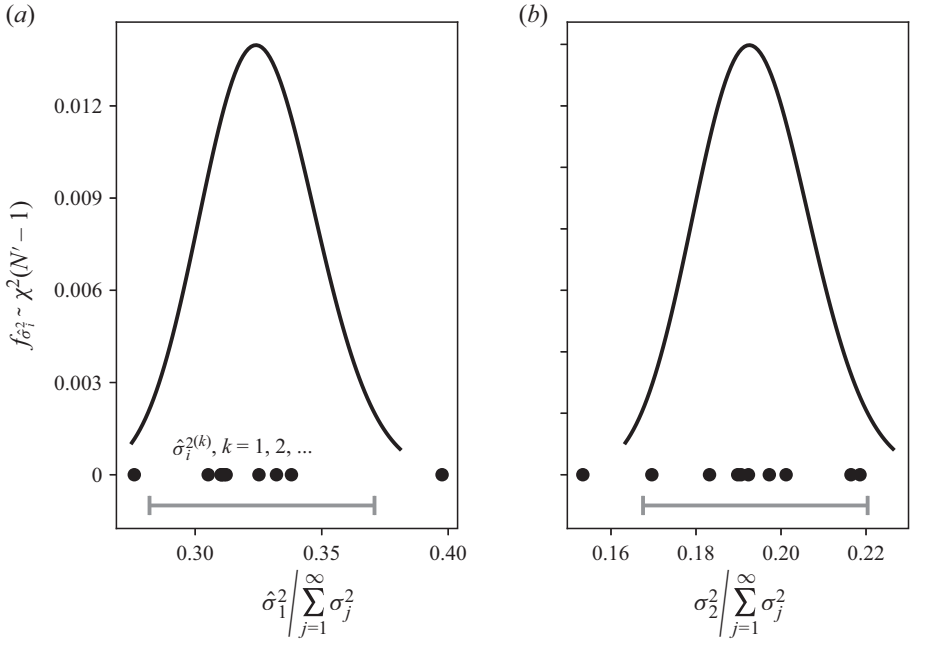

Figure 5. Estimation of the variance of the leading principal component time series. Black dots correspond to point estimators computed from the individual runs, which vary according to the associated sampling distribution. The grey error bars indicate the 95 % confidence intervals over all runs, centred around the POD eigenvalues (cf. figure 4*a*).

and

$$\hat{\sigma}^2 = \int_{-\infty}^{+\infty} (x - \hat{\mu})^2 \, \mathrm{d}\hat{F}(x) = \frac{1}{N} \sum_{n=1}^{N} (x_n - \hat{\mu})^2, \tag{5.6}$$

respectively. For samples drawn from a Gaussian distribution (as we show in § 5.4), these definitions of the sample mean and variance correspond to the maximum likelihood estimates (Cramér 1963; von Storch & Zwiers 2003). From § 4.2, we recall that $\hat{\mu}$ and $\hat{\sigma}^2$ are random numbers. Their quality in estimating the true (deterministic) population values μ and σ^2 depends on the associated sampling distributions. This is shown in figure 5, where black dots correspond to the different variance estimates computed on different, identically prepared runs of the experiment. Obviously, no reliable statement about the true meandering variance can be obtained from particular realisations of the sample variance, which scatter according to the sampling distribution. To have a robust result, we define the test statistic

$$\mathfrak{x} := \frac{N' \hat{\sigma}_i^2}{\sigma_i^2} \sim \chi^2(N' - 1) \tag{5.7}$$

as multiples of the unknown population value. If the sample is drawn from a Gaussian distribution, then the non-dimensional variance defined in (5.7) has a χ^2 sampling distribution with $N' - 1$ degrees of freedom (Cramér 1963; von Storch & Zwiers 2003). To account for serial correlation of the data, we use the equivalent sample size $N_i' = 410$ ($i = 1, 2$), computed with the decorrelation time (4.3).

Given the confidence level $\tilde{p}$ and degrees of freedom $N' - 1$, we readily obtain the interval bounds $(\mathfrak{x}_{\tilde{p}}^L, \mathfrak{x}_{\tilde{p}}^U)$ from $\tilde{p} = P_{\chi^2(N'-1)}(\mathfrak{x}_{\tilde{p}}^L < \mathfrak{x} < \mathfrak{x}_{\tilde{p}}^U)$. Thus, the unknown

population variance is covered by the confidence interval

$$\left(\frac{N'\hat{\sigma}_i^2}{\mathfrak{k}_{\tilde{p}}^U}, \frac{N'\hat{\sigma}_i^2}{\mathfrak{k}_{\tilde{p}}^L}\right) \quad \text{at the } \tilde{p} \times 100\,\% \text{ level of confidence.} \tag{5.8}$$

Figure 5 shows the confidence interval (5.8) that contains the true value of the variance in 95 % of the cases if we were to repeat the same experiment infinitely often. Overlaying these confidence intervals on figure 4(*a*) of the POD eigenvalue spectrum, we find that they overlap with the North *et al.* (1982) rule of thumb (5.4*a*,*b*). The latter being computed with a Gaussian sampling distribution implies that our experiment corresponds to an asymptotically large sample.

From § 3.3, we recall that our vortex meandering model predicts the variance to grow as

$$\frac{\sigma_i^2(t)}{U_\infty^2} \sim 2\left(\frac{u}{U_\infty}\right)^2 \frac{t}{t_s} \quad (i = 1, 2), \tag{3.16}$$

where $u/U_\infty \approx 5 \times 10^{-3}$ denotes the turbulence intensity of the experimental facility (§ 2.1). Further, recalling our estimate $t_s/t_a \sim 10$ of the slow vortex response time scale from § 3.2, our theoretical model predicts standard deviation growth according to

$$\frac{\sigma_i(t)}{U_\infty} \sim 2 \times 10^{-3}\sqrt{\frac{t}{t_a}} \quad (i = 1, 2) \tag{5.9}$$

for the present experimental parameters. Standard deviation growth according to (5.9) is displayed in figure 6, along with the corresponding standard deviation point estimators (5.6) and 95 % confidence intervals (5.8) in the available measurement planes. The equivalent sample size in the last three measurement planes is similar in magnitude to the above given value $N_i' = 410$. However, the autocorrelation structure of the dynamics is shorter in the first two measurement planes, which results in larger equivalent sample sizes here, which explains the narrower confidence intervals in the first two measurement planes. Physically, this finding means that the temporal signature of vortex meandering in measurement planes close to the vortex generator is close to white noise, while a significant correlation structure establishes only beyond $z/c \sim 10$ for the given experimental parameters (see the Appendix). This downstream amplification of vortex meandering is a well-known experimental fact (Baker *et al.* 1974; Devenport *et al.* 1996; Edstrand *et al.* 2016). Overall, we find that our model (5.9) corresponds reasonably well with the available point estimators, and stays within the 95 % confidence interval. An amplification according to (5.9) was explicitly reported in previous studies (van Jaarsveld *et al.* 2011; Bailey *et al.* 2018; Dghim *et al.* 2021) and was shown to be consistent with a broad range of experiments (Bölle 2021, 2023).

5.3. *Stationarity of vortex meandering*

Likely the usual and simplest way to infer stationarity of a random sample is by considering the underlying physics of the phenomenon relative to which the data have been taken, together with the measurement instructions detailing the sampling process (Bendat & Piersol 2010). In experiments, we expect stationarity of the data by taking measurements after initial transients due to start-up of the facility have died out. Indeed, visual inspection of the sample time series shown in figure 1 does not reveal any obvious non-stationarity such as trends or periodicities. As required for stationary time series, all anomalies are

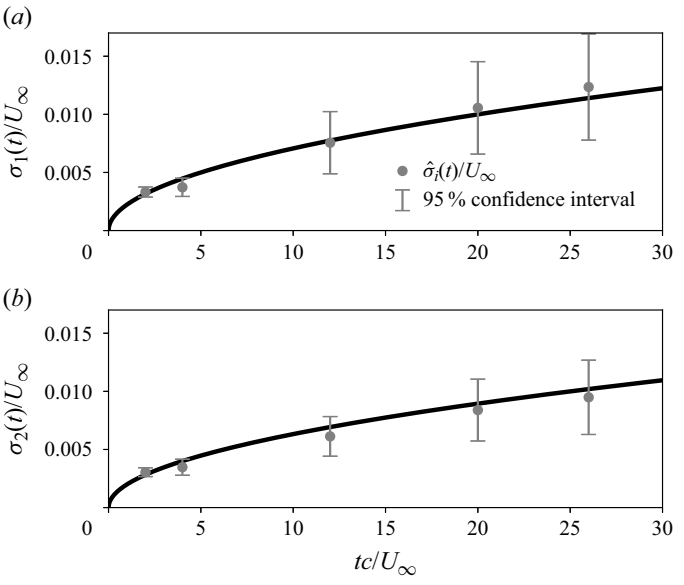

Figure 6. Downstream amplification of the vortex meandering standard deviation. Point estimates and 95 % confidence intervals for the five measurement planes are shown in grey, where the thick black line illustrates the predicted growth according to the Brownian-motion-like meandering model (5.9). Besides the second measurement plane, the model consistently stays in the range spanned by the 95 % confidence intervals, and closely matches the point estimates.

necessarily temporary, returning to zero eventually. Finite duration of the anomalies is consistent with decay of the autocorrelation function shown in figure 10 below. Although there is no obvious indication for non-stationarity of the sample, autocorrelations close to unity ($\hat{\rho}_1 := \exp(-\hat{\lambda}_1\,\Delta t) = 0.990$ here; see § 5.5) imply that we should principally be concerned about stationarity (Enders 1995). In this subsection, we use a hypothesis test to quantitatively show data stationarity.

To this end, we conjecture that meandering in fact corresponds to a non-stationary process, and show that the actually realised sample deviates significantly from this null hypothesis. We suppose that the sample time series is generated from a slowly varying first-order process

$$x_t = a x_{t-1} + \epsilon_t, \tag{5.10}$$

where ϵ_t is a stationary white noise process, and $|a| < 1$ guarantees stationarity of the $\{x_t\}$ sequence (Enders 1995; Wilks 2006). This is consistent with our model (cf. § 3), as the process defined by (5.10) corresponds to a discrete form of an Ornstein–Uhlenbeck process that is stationary if we take $x_0 = x(t \to -\infty)$ as the initial condition. Letting now $|a| = 1$, recursively applying (5.10) yields

$$x_t = x_{t-1} + \epsilon_t = x_{t-2} + \epsilon_{t-1} + \epsilon_t = \cdots = x_0 + \sum_{i=1}^{t} \epsilon_i. \tag{5.11}$$

For the variance of this unit-root process, we readily derive

$$V(x_t - x_0) = V\left(\sum_{i=1}^{t} \epsilon_i\right) = \sum_{i=1}^{t} V(\epsilon_i) = \sigma_\epsilon^2 t, \tag{5.12}$$

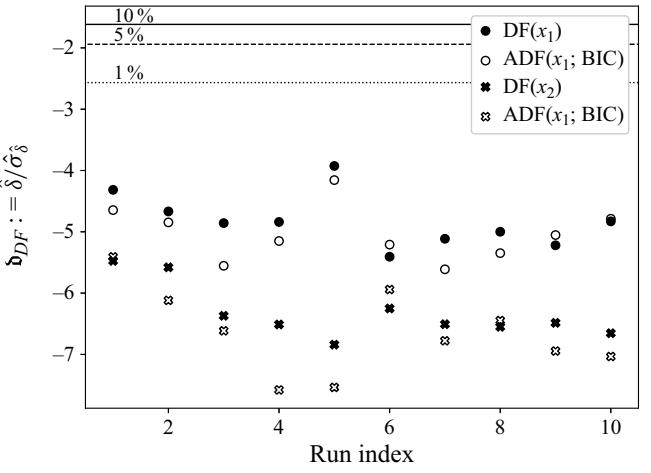

Figure 7. Results of the Dickey–Fuller (DF) test for each run, showing stationarity of the leading two principal components $x_1(t), x_2(t)$ at the 1 % level of significance (filled markers). Stationarity at the 1 % level of significance also holds for the augmented Dickey–Fuller (ADF) test with optimal lag determined by the Bayesian information criterion (BIC) (respective open markers). The 1 % to 10 % levels of significance are shown by dotted, dashed and solid lines, respectively.

using the fact that the elements of a white noise process are mutually uncorrelated and stationary with variance σ_ϵ^2. Equation (5.12) reflects the well-known result that summing over a stationary random process ϵ_t yields a non-stationary random process x_t (Yaglom 1962). Recognising that (5.11) is a Wiener process, this is also plausible on physical grounds.

Statistical tests of stationarity that are based on this reasoning are called unit-root tests. A suitable variant for our purposes is the Dickey–Fuller test (Hamilton 1994; Enders 1995), which is based on the difference equation

$$\Delta x_t = x_t - x_{t-1} = (a-1)x_{t-1} + \epsilon_t = \delta x_{t-1} + \epsilon_t, \tag{5.13}$$

obtained from subtracting x_{t-1} on both sides of (5.10). Taking the null hypothesis that the sample sequence $\{x_t\}$ is generated from a non-stationary process implies that we have to test for $H_0 : \delta = 0$. We thus define the Dickey–Fuller test statistic $\mathfrak{d}_{DF} := \hat{\delta}/\hat{\sigma}_\delta$ as the deviation of the estimator $\hat{\delta}$ from the expected value $\delta = 0$ as multiples of the standard error $\hat{\sigma}_\delta$. Test thresholds are tabled in Enders (1995). Figure 7 shows that the sample principal component time series obtained from the ten measurement runs (cf. § 2.1) are stationary at the 1 % level of significance.

We used the Dickey–Fuller test here as it corresponds to our meandering model. Figure 7 also includes the respective results for the augmented Dickey–Fuller test. The latter generalises (5.10) to a p-order process, where the number of lags p is determined by the Bayesian information criterion (see also Enders 1995; Wilks 2006). From figure 7, we see that stationarity of the leading sample principal component time series also holds for the augmented Dickey–Fuller test at the 1 % level of significance.

We conclude that vortex meandering in the given experiment (§ 2.1) is a stationary process in a fixed measurement plane.

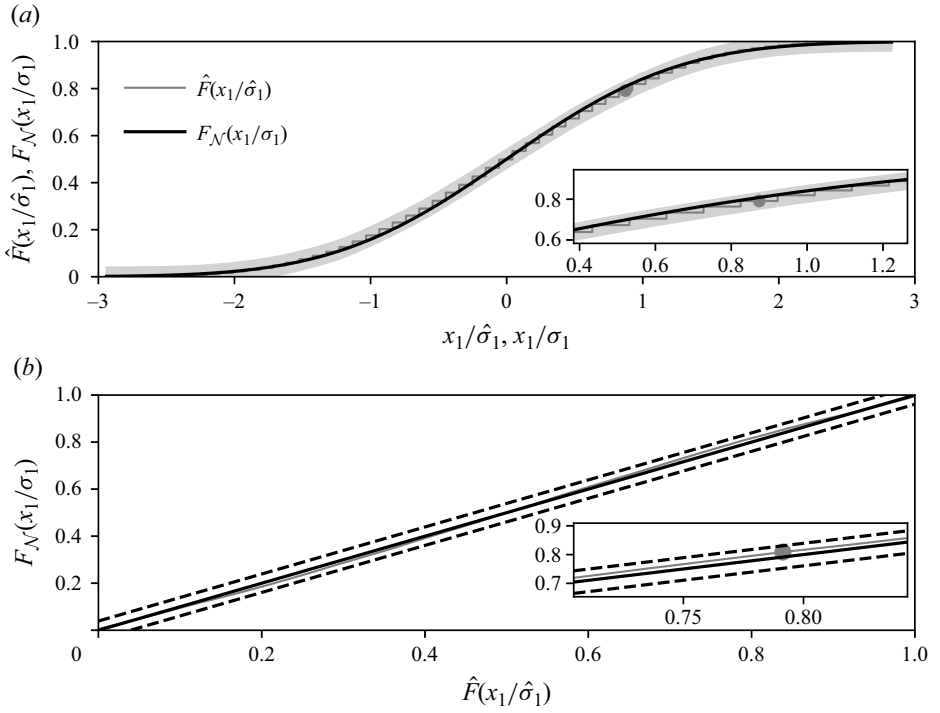

Figure 8. Comparison of the standardised empirical distribution $\hat{F}_{X_1}$ with the standard Gaussian distribution $F_{\mathcal{N}}$. (*a*) A 60 bins histogram of $\hat{F}_{X_1}$ compared with a Gaussian distribution, including the 95 % confidence interval (grey shading). The inset shows a close-up of the region of largest deviation (indicated by a grey dot) from the Gaussian distribution. (*b*) Standard normal distribution over empirical distribution $(\hat{F}_{X_1}, F_{\mathcal{N}})$ (bold grey). An exact Gaussian distribution would collapse with the diagonal (thin black). Dashed off-diagonals are the thresholds for the hypothesis, the sample is normally distributed, to be rejected at the 5 % significance level.

5.4. *Gaussian distribution of vortex meandering*

The estimator $\hat{F}_{X_i}(x_i)$ of the distribution function of the sample $F_{X_i}(x_i)$, called the empirical distribution function, is defined as

$$\hat{F}_{X_i}(x_i) := \frac{\mathrm{card}(\{X_i^{(n)} \,:\, X_i^{(n)} \leq x_i\})}{N} \quad (i = 1, 2), \tag{5.14}$$

where $\mathrm{card}(A)$ is the cardinality of the set A (Cramér 1963; von Storch & Zwiers 2003). We notice that since the relative counts in each bin of (5.14) depend on the sample $\boldsymbol{x}_N$ actually realised, $\hat{F}_{X_i}(x_i)$ is in fact a random variable, as all estimators (cf. § 4.2). The histograms (assuming 60 bins) corresponding to the estimator defined in (5.14) are shown in figures 8 and 9 for the leading two principal components. Analogous results for the upstream measurement planes are shown in the Appendix.

While figures 8 and 9 show fair agreement between theory and experiment, histograms or frequency distributions are crude estimates in general (von Storch & Zwiers 2003). We therefore rely on statistical tests, which for probability distributions are typically called goodness-of-fit tests. To this end, we suppose that the population distribution function is Gaussian, i.e. we assume the null hypothesis $H_0 : F_{X_i}(x_i) = F_{\mathcal{N}}(x_i), F_{\mathcal{N}}(x_i) = (1/2\pi) \int_{-\infty}^{x_i} \mathrm{d}z \exp(-z^2/2)$.

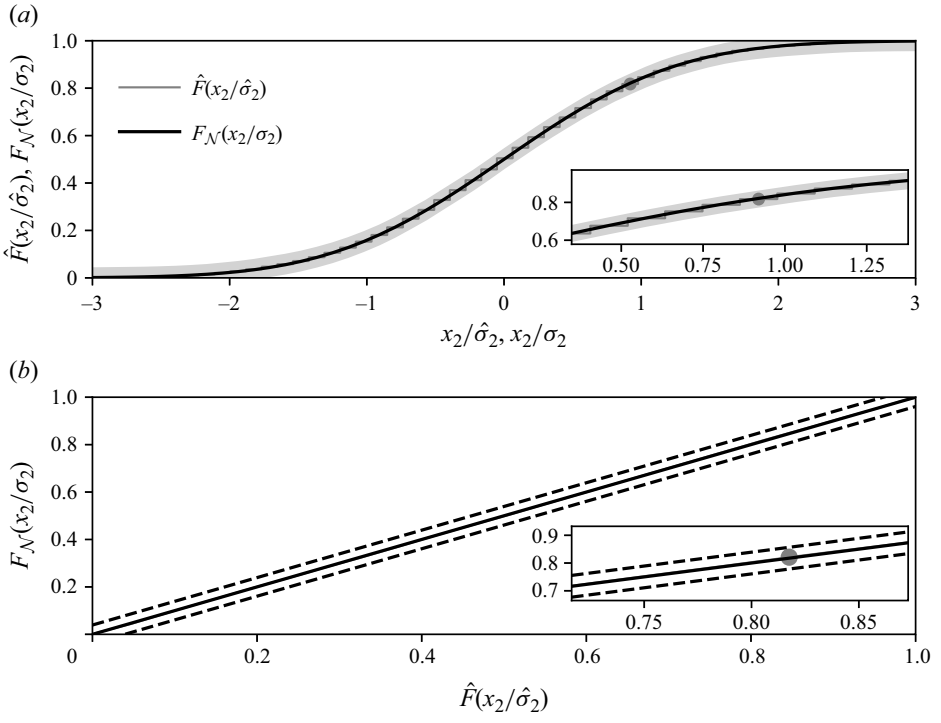

Figure 9. Comparison between the standardised sample distribution $\hat{F}_{X_2}$ and the standard normal probability distribution $F_{\mathcal{N}}$. See figure 8 for details.

In order to assess closeness of the empirical distribution function to a Gaussian distribution, we use the Kolmogorov–Smirnov test (Wilks 2006). To understand this test, recall that as the number of elements in each bin as well as the bins themselves tend to infinity, the estimator (5.14) converges (almost surely) to the population distribution function by the Glivenko–Cantelli theorem (Cramér 1963). This suggests using the uniform norm as a distance measure

$$\mathfrak{d}_{KS} := \max_{x \in \boldsymbol{x}_N} |\hat{F}_X(x) - F^*_{\mathcal{N}}(x)|, \tag{5.15}$$

referred to as the Kolmogorov–Smirnov test statistic. Strictly speaking, the Kolmogorov–Smirnov test applies only if the true distribution parameters are known (Lilliefors 1967). Using estimators instead, as we do, is indicated by adding an asterisk to the conjectured population distribution in (5.15). Appropriately modified test bounds for the Kolmogorov–Smirnov test statistic (5.15) have been computed by Lilliefors (1967) (see also von Storch & Zwiers 2003; Wilks 2006).

The critical values for the Lilliefors test depend on the sample size N. As discussed in § 4.3, due to serial correlation of the data, we have to consider the effective sample size N' instead, which depends on the statistical characteristic that is estimated. Lanzante (2021) suggests using (4.2) for a first-order autoregressive process to compute N' for the empirical distribution function.

Here, we propose the following estimate. The Kolmogorov–Smirnov test statistic (5.15) defines a distance measure between the empirical and population distribution functions in terms of the uniform norm. Among the various other metrics that can

be defined (e.g. Cramér 1963), we know that the variance is given by $V(\hat{F}_X(x)) = F_X(x)\,(1 - F_X(x))/N$ for any empirical distribution function (von Storch & Zwiers 2003). Motivated by general norm inequalities, we expect that $\mathfrak{d}_{KS}^2 \geq V(\hat{F}_X(x^*))$, letting $x^* = \arg\max_{x \in \boldsymbol{x}_N} \mathfrak{d}_{KS}$. The point of maximal deviation x_i^* in the uniform norm is indicated by a grey dot in figures 8 and 9. For the sake of estimating N', we assume that $\mathfrak{d}_{KS}^2 = V(\hat{F}_X(x^*)) = F_{\mathcal{N}}^*(x^*)\,(1 - F_{\mathcal{N}}^*(x^*))/N'$, which yields $N' = F_{\mathcal{N}}^*(x^*)\,(1 - F_{\mathcal{N}}^*(x^*))/\mathfrak{d}_{KS}^2$ as an estimate of the equivalent sample size. For the present experiment, we thus obtain the estimated value $N' = 510$ for the equivalent sample size.

Taking this estimate for N', as shown in figures 8(*b*) and 9(*b*), the leading sample principal components are consistent with a Gaussian distribution at the 5 % level of significance. In agreement, figures 8(*a*) and 9(*a*) show that the 95 % confidence interval of the empirical distribution consistently covers the conjectured Gaussian distribution.

This finding has a noteworthy implication on the nature of the meandering dynamics (Bölle 2021). If meandering was indeed governed by a genuine instability or transient-growth mechanism, then the dominant vortex response should be a helical wave. The corresponding probability distribution would then be M-shaped, with peaks around the oscillation amplitude (Tennekes & Lumley 1972). This conclusion is confirmed by direct numerical simulations (DNS) of the nonlinear vortex dynamics initialised with optimal perturbations (Mao & Sherwin 2012; Navrose & Jacquin 2019). Obviously, the experimentally observed probability distribution differs significantly from this conjecture and must be rejected. We further emphasise that the oscillatory vortex response observed in DNS does not correspond to the initial phase of transient energy amplification due to non-normal linear dynamics, but occurs in the nonlinear saturation regime (Mao & Sherwin 2012; Navrose & Jacquin 2019; Bölle 2021). We therefore conclude that vortex meandering, in the given experiment, differs significantly from a helical motion as predicted by a genuine instability or transient-growth mechanism. This is already emphasised clearly by Bailey & Tavoularis (2008) and Bailey *et al.* (2018).

5.5. *Sample correlation in the vortex meandering manifold*

In the preceding subsection we concluded that the hypothesis of vortex meandering corresponding to a dominant helical wave must be rejected. This association with a deterministic wave motion clearly understands vortex meandering as a purely intrinsic dynamics, and implies the existence of a governing 'meandering frequency' (or wavelength). Due to its direct relation to instability mechanisms, the quest for a characteristic meandering frequency has been attempted repeatedly (Devenport *et al.* 1996; Jacquin *et al.* 2001; Bailey & Tavoularis 2008; Roy & Leweke 2008; Bailey *et al.* 2018). However, the identification of 'hidden periodicities' in random samples of finite size is not obvious (Fuller 1996; von Storch & Zwiers 2003). In this and the following subsection, by systematic application of the tools introduced in § 4, we inquire whether there is significant evidence for the existence of a dominant meandering frequency in the present experiment.

Several definitions of the correlation function estimator exist (Trenberth 1984; Fuller 1996). If the expectation is unknown, then the prevalent gives rise to the sample correlation (Abraham & Ledolter 1983; Hamilton 1994; Enders 1995; Fuller 1996)

$$\hat{\rho}_{ij}(\nu) = \frac{1}{N}\sum_{n=1}^{N-\nu} \frac{(x_i(n) - \bar{x}_i)(x_j(n+\nu) - \bar{x}_j)}{\hat{\sigma}_i \hat{\sigma}_j}, \quad \nu = 0, 1, 2, \ldots, N-1. \tag{5.16}$$

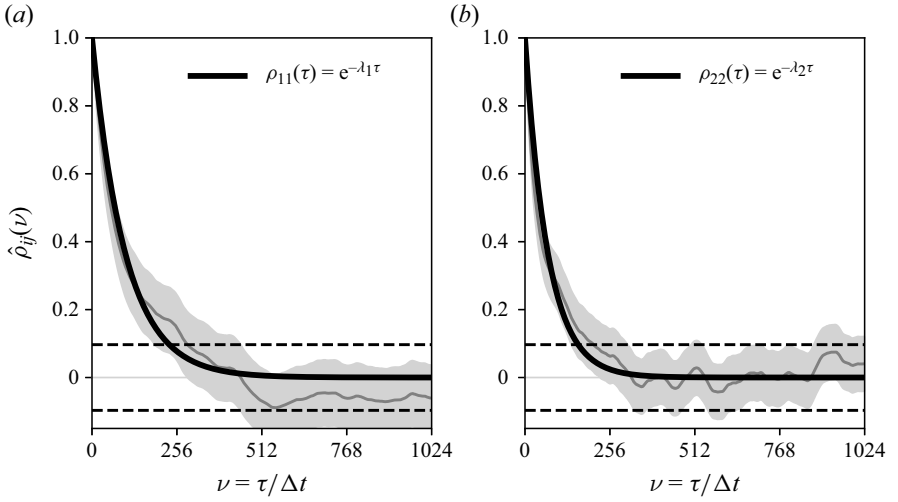

Figure 10. Autocorrelation functions of the first and second principal component time series. For sample correlations (grey line) outside the dashed horizontal lines, the null hypothesis of the signal being uncorrelated is rejected at the 5 % level of significance. Grey shading around the sample correlations indicates the 95 % confidence intervals, which overlap with the conjectured exponential autocorrelation of the population.

Strictly speaking, (5.16) is neither the maximum likelihood nor the least squares estimator; see Fuller (1996) for further discussion.

Figures 10 and 11 show the different time-lagged sample correlations (5.16) computed from the experimental data. Although we find fair agreement with the conjectured theoretical correlations (3.17) in all cases, the sample correlations are subject to fluctuations, which could be indicative of periodicities in the meandering dynamics not covered by the model. On the other hand, spurious variability of the sample correlations, in particular at large time lags, is a consequence of the finiteness of the sample (von Storch & Zwiers 2003). In this subsection, we inquire whether these apparently oscillatory fluctuations are statistically significant or merely an artefact of working with finite samples.

In order to test for serial correlation in the principal component time series, we conjecture the null hypothesis $H_0 : \rho_{ij}(\nu) = 0$, i.e. that the data in the sample are uncorrelated, and use the von Neumann ratio

$$\mathfrak{d}_{ij} := \frac{\sum_{n=2}^{N} (x_i(n) - x_j(n-1))^2}{\sqrt{\sum_{n=1}^{N} x_i^2(n)} \sqrt{\sum_{n=1}^{N} x_j^2(n)}} \approx 2(1 - \hat{\rho}_{ij}(1)) \quad (i, j = 1, 2) \tag{5.17}$$

as a test statistic. We recognise that (5.17) is essentially an adaptation of the Durbin–Watson test for regression residuals (Fuller 1996; von Storch & Zwiers 2003). From (5.17), we see that the test statistic takes values $\mathfrak{d} \in [0, 4]$, where perfectly uncorrelated time series are associated with a test statistic $\mathfrak{d} = 2$, while values $\mathfrak{d} \to 0$ indicate progressively stronger positive autocorrelation. Evaluating (5.17) for the leading two principal component time series of the experiment yields $\mathfrak{d}_{11} = 0.05$, $\mathfrak{d}_{22} = 0.08$ and $\mathfrak{d}_{12} = \mathfrak{d}_{21} = 2.00$. That is, on the basis of this test, we cannot reject H_0 for the time-lagged cross-correlations, while the respective time series have significant positive autocorrelations, respectively (Hart 1942).

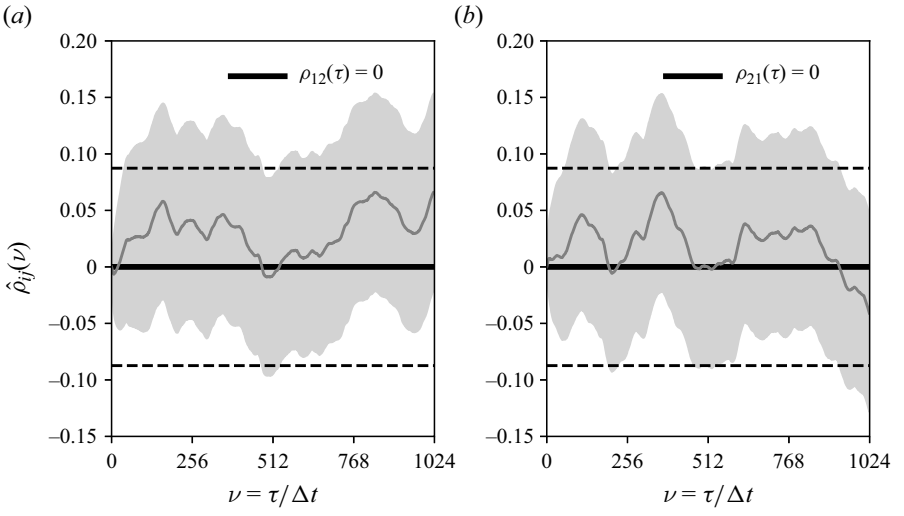

Figure 11. Cross-correlations of the first and second principal component time series. See figure 10 for details.

This finding is corroborated by recalling that for large sample sizes drawn from a Gaussian distribution, the correlation estimate (5.16) has an approximately Gaussian sampling distribution (Cramér 1963; Fuller 1996; Wilks 2006). Hence, testing for the null hypothesis that principal component time series pertaining to the same or different POD modes are uncorrelated amounts to comparing $|\hat{\rho}_{ij}(\nu)|$ with its Gaussian standard error (Abraham & Ledolter 1983; Wilks 2006). If the sample is drawn from a stationary Gaussian process (cf. §§ 5.3–5.4) with vanishing correlation beyond lag p, then the variance of the sample correlation is approximately (Abraham & Ledolter 1983; Fuller 1996; von Storch & Zwiers 2003)

$$V(\hat{\rho}_{ij}(\nu)) \approx \frac{1}{N}\left(1 + 2\sum_{n=1}^{p} \hat{\rho}_{ii}(\nu)\,\hat{\rho}_{jj}(\nu)\right), \quad \nu > p. \tag{5.18}$$

We thus define the standardised Gaussian test statistic $\mathfrak{z} := \hat{\rho}_{ij}(\nu)/\hat{\sigma}_{\hat{\rho}_{ij}}$ (denoting $\hat{\sigma}_{\hat{\rho}_{ij}} = V(\hat{\rho}_{ij}(\nu))$), and reject H_0 at the $\tilde{p} \times 100\,\%$ level of significance if

$$\sqrt{N'}\,|\hat{\rho}_{ij}(\nu)| > \mathfrak{z}^{\pm}_{\tilde{p}}, \quad \nu > 0, \tag{5.19}$$

with $\mathfrak{z}^{\pm}_{\tilde{p}} = 1.96$ for $\tilde{p} = 0.05$. In (5.19), we have used that (5.18) corresponds to the reciprocal equivalent sample size (4.1*a*,*b*) computed with the decorrelation time (4.4). We notice that in (5.19), $N' \to N$ if the data have no serial correlation. Figures 10 and 11 contain the bounds on the test statistic (5.19) corresponding to the 5 % significance level as dashed lines.

Both tests, based on (5.17) and (5.19), show that the individual principal component time series have significant autocorrelation for sufficiently short time lags ($\nu \lesssim 256$), while they are mutually uncorrelated at all time lags. We emphasise that the mathematical properties of the POD merely impose vanishing cross-correlations at zero time lags (Holmes *et al.* 1996).

Our findings so far do not immediately imply any particular autocorrelation structure. In order to provide evidence for the appropriateness of our model (3.17), we further show

that the correlation interval estimators overlap with the respective conjectured theoretical correlations; cf. figure 10. Using the above results, the population correlation function $\rho_{ii}(\nu)$ is covered by the $(1-\tilde{p})\times 100\,\%$ confidence interval (Abraham & Ledolter 1983)

$$\hat{\rho}_{ii}(\nu) \pm \frac{\mathfrak{z}_{\tilde{p}}^{\pm}}{N}\left(1+2\sum_{n=1}^{\nu-1}\hat{\rho}_{ii}^{2}(\nu-1)\right), \quad \nu>0. \tag{5.20}$$

Trivially, $\hat{\rho}_{ii}(0)=1$ is non-random and consequently collapses with its confidence interval. We take the finding that the 95 % confidence interval contains the model autocorrelation at all time lags, shown in figure 10, as sufficient evidence for the appropriateness of our model. In particular, the entire variability of the correlation structure is spurious at this level, and cannot be related significantly to any periodicity of the dynamics.

A stationary Gauss process is Markovian if and only if it has exponential autocorrelation (Yaglom 1962). On account of our statistical analyses of the experimental data in §§ 5.3–5.5, we therefore reach the important conclusion that vortex meandering corresponds to a Markov process. This confirms our Brownian-motion-like meandering model (§ 3) for the given experiment at the 5 % level of significance.

5.6. *Sample Eulerian time spectrum*

To corroborate our previous conclusion that the meandering dynamics in the given experiment is not significantly associated with any (hidden) periodicity, we discuss the power spectra in this subsection (see also the Appendix). There is a persistent practice to compare power spectra of supposedly turbulent flow with the well-known power-law slopes of either two- or three-dimensional turbulence (Tennekes & Lumley 1972; Devenport *et al.* 1996; Jacquin *et al.* 2001; Bailey & Tavoularis 2008). However, these power laws hold in the inertial range, while vortex meandering is associated with the integral, energy-carrying scales. In fact, our Langevin model implies the power-spectral signature (3.17), as shown in figure 12.

The Wiener–Khinchin theorem (2.6*a*,*b*) suggests estimating the power spectrum by taking the Fourier transform of the estimated autocovariance functions. This direct approach yields the periodogram, which is known to be a poor spectral estimator (von Storch & Zwiers 2003). Rather, we estimate the power spectrum by Welch's average periodogram method (Welch 1967). To this end, we split the principal component time series into K overlapping segments, compute the modified periodogram from each segment, and estimate the power spectrum by averaging all periodograms. Given a time series of length $N=40\,960$ in the experiment, we define each segment to contain $N_b=4096$ contiguous data points. Allowing an overlap of $1-D=0.5$ between adjacent segments, as suggested by Welch (1967), the time series are covered by $K=19$ overlapping segments.

We define the normalised spectral estimator as (von Storch & Zwiers 2003; Bendat & Piersol 2010)

$$\mathfrak{x} := \frac{2K_D\,\hat{G}_{ii}(\omega)}{G_{ii}(\omega)} \sim \chi^2(2K_D), \tag{5.21}$$

where $2K_D$ denotes the equivalent degrees of freedom of the χ^2 distribution, given approximately by $2K_D \approx 18K/11 \approx 31$ (Welch 1967). Welch's correction of the degrees of freedom accounts for variance inflation of the spectral estimate due to overlapping

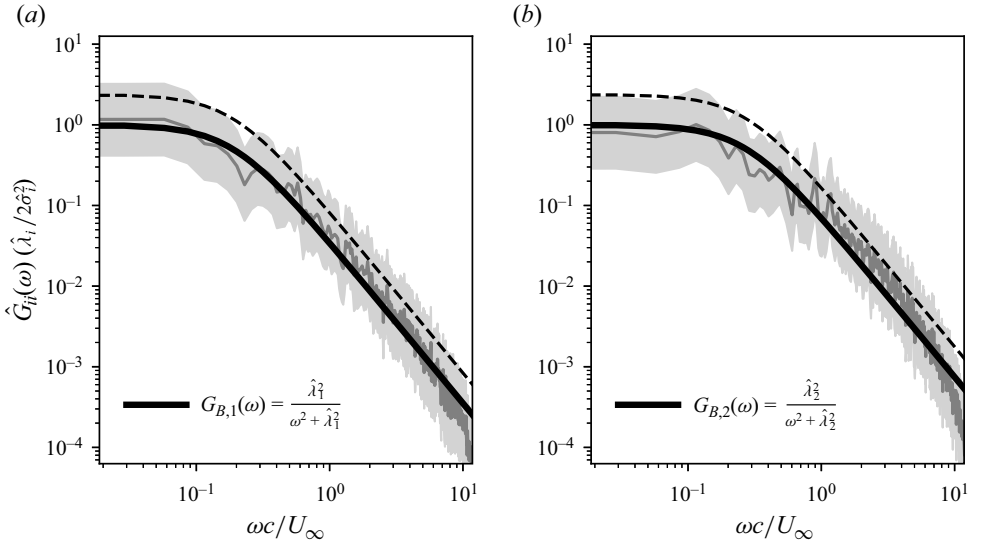

Figure 12. Power spectra of the first and second principal component time series. Spectral estimates $\hat{G}_{ii}(\omega)$ (grey lines) and their respective 95 % confidence intervals (grey shading) overlap with the conjectured population power spectra (solid black lines). Dashed black lines indicate the 5 % significance level bounds (5.24) to reject the null hypothesis that no preferred frequency exists.

segments, reducing to $2K_D \to 2K$ for non-overlapping segments of Bartlett's method (von Storch & Zwiers 2003). Letting $\mathfrak{x}_{\tilde{p}}^L, \mathfrak{x}_{\tilde{p}}^U$ denote the limiting values of the $\chi^2(2K_D)$ distribution, such that $\tilde{p} = P_{\chi^2}(\mathfrak{x}_{\tilde{p}}^L \leq \mathfrak{x} \leq \mathfrak{x}_{\tilde{p}}^U)$, the true population spectrum is covered by the confidence interval

$$G_{ii}(\omega) \in \left(\frac{2K_D\,\hat{G}_{ii}(\omega)}{\mathfrak{x}_{\tilde{p}}^U}, \frac{2K_D\,\hat{G}_{ii}(\omega)}{\mathfrak{x}_{\tilde{p}}^L} \right) \quad \text{at the } \tilde{p} \times 100\,\% \text{ level of confidence.} \tag{5.22}$$

Figure 12 shows the estimated power spectra of the leading principal component time series. Overlapping of the corresponding 95 % confidence intervals (5.22) with the conjectured model power spectra (3.17) provides evidence for the validity of the meandering model.

For the normalisation of the power spectra, recall that $\int_{\mathbb{R}} \mathrm{d}\omega\, G_{ii}(\omega) = \sigma_i^2$ by Parseval's theorem (Yaglom 1962). This implies that the normalised power spectra $\hat{G}_{ii}(\omega)/\hat{\sigma}_i^2$ represent the partial variance contained in the frequency interval $\mathrm{d}\omega$ around ω. Observing that $\hat{G}_{ii}(\omega)/\hat{\sigma}_i^2$ always has the dimension of a time, irrespective of the dimension of the underlying random process, requires further normalisation on a characteristic time scale to obtain a dimensionless result. Our analysis so far suggests taking (twice) the vortex response time scale $2\hat{\lambda}_i^{-1}$, which amounts to the normalisation $\hat{G}_{ii}(\omega)/\hat{G}_{ii}(0)$ (von Storch & Zwiers 2003). Evaluating the power spectrum at $\omega = 0$, we obtain $G_{ii}(0)/\sigma_i^2 \sim \int_{\mathbb{R}} \mathrm{d}\tau\, \rho_{ii}(\tau) = 2\lambda_i^{-1}$, recalling that λ_i^{-1} equals the integral time scale (Yaglom 1962; Tennekes & Lumley 1972). Figure 12 shows that the normalised spectral estimates are close to unity as $\omega \to 0$. The normalised model power spectra (3.17) proceed along the same lines to yield $G_{B,i}(\omega) = \lambda_i^2/(\omega^2 + \lambda_i^2)$. Obviously, $G_{B_i}(\omega \to 0) \to 1$, as can also be seen in figure 12.

As discussed in § 1, vortex meandering is repeatedly assumed to be associated with some preferred frequency of the order of $fc/U_\infty \sim 1$. Indeed, if one such meandering frequency exists, then it would show up as a peak in the spectral estimates. On the other hand, it is well known that power spectra computed from finite samples are subject to erratic peaks. The sample power spectra shown in figure 12 display several such potential peaks. Taking a decision on a statistical basis, we consider any peak as significant that has significantly larger variance than the conjectured model power spectrum. Our meandering model assumes a red noise power spectrum (3.17), which is known to admit no preferred frequency. Thus, a suitable statistical test for the existence of any preferred meandering frequency is readily constructed by assuming the null hypothesis that the population has a red noise power spectrum, i.e. $H_0 : G_{ii}(\omega) = G_{B,i}(\omega)$. Assuming (5.21) as the test statistic, a frequency ω_j is significant at the $1 - \tilde{p}$ level if for the associated squared amplitude estimate $\hat{A}_j^2$ we have (Wilks 2006)

$$\hat{A}_j^2 \geq \frac{G_B(\omega_j)}{2K_D}\, \text{ɮ}_{\tilde{p}}^U, \quad \text{where } \text{ɮ}_{\tilde{p}}^U : P_{\chi^2(2K_D)}(\text{ɮ} \geq \text{ɮ}_{\tilde{p}}^U). \tag{5.23}$$

The test (5.23) is appropriate for *a priori* known frequencies, whereas if no such frequency is specified beforehand, then we must account for test multiplicity by the Bonferroni method, yielding the modified test criterion (Wilks 2006)

$$\hat{A}_j^2 \geq \frac{G_B(\omega_j)}{2K_D}\, \text{ɮ}_{\tilde{p}^*}^U \quad \text{where } \tilde{p}^* = 1 - \alpha^* = 1 - \frac{2\alpha}{N_b}. \tag{5.24}$$

In (5.24), $N_b/2 = 2048$ is the number of frequencies in the estimator, and $\alpha^* = 5 \times 10^{-2}$ and $\alpha \approx 2.4 \times 10^{-5}$ are the nominal and actual test levels, respectively. The dashed lines in figure 12 display the squared amplitude threshold resulting from (5.24), beyond which the null hypothesis that there exists no preferred frequency can be rejected at the 5 % level of significance. Since the sample power spectra always remain below this threshold, we conclude that vortex meandering, at least in the present experiment, is not associated with any distinguished characteristic frequency at the given level of significance.

5.7. *Ergodicity of vortex meandering*

Taking measurements after initial transients have died out, we tacitly assume the dynamics to be characterised by an ergodic probability measure. Thus, taking time averages (as we did throughout) is asymptotically equivalent to computing expectations from the equilibrium ensemble. As is well known, a stochastic process can be ergodic only if it is also stationary (Bendat & Piersol 2010), shown to be true in § 5.3. According to Hänggi & Thomas (1982), finite values of the power spectra as $\omega \to 0$ further constitute a sufficient condition for ergodicity. This was shown to be the case in figure 12 of § 5.6. As a matter of fact, ergodicity holds for the class of stationary, Gaussian random processes having absolutely continuous power spectra, i.e. having no discrete frequencies associated with distinct periodicities (Bendat & Piersol 2010). In §§ 5.3–5.6, we provided statistical evidence that vortex meandering corresponds to a stationary Gauss–Markov process, being a subset of this class. We therefore conclude that vortex meandering in the experiment is ergodic.

6. Conclusion

Meandering constitutes the main manifestation of vortex unsteadiness commonly observed in experiments, and serves as the prototype of the slow vortex response dynamics.

In this study, we review previous approaches at explaining the phenomenon, and develop a unified stochastic model in the context of linear response theory. The resulting theory identifies experimental vortex meandering as a form of Brownian motion, and is the first model that is consistent with all fundamental characteristics observed universally in experiments, namely (i) the Gaussian distribution of the vortex position with (ii) growing slow-scale variance downstream and (iii) the broadband power spectral signature.

The statistical identification of characteristic features in experimental data and relating them to theoretical models are ubiquitous problems in physics. However, past fluid dynamics studies regularly resorted to qualitative comparisons and subjective judgements in the interpretation of statistical characteristics. In the present study, we introduce an objective statistical methodology for the systematic and quantitative characterisation of experimental data relative to theoretical models. While this framework is of basic relevance for fluid dynamics experiments in general, we discuss its application to a prototypical problem in experimental vortex dynamics. This allows us to robustly identify experimental vortex meandering with our proposed Brownian-motion-like model at a precisely specified level of certainty.

In particular, working at the 5 % level of significance, we provide statistical evidence that vortex meandering observed in experiments constitutes the manifestation of a stationary Gauss–Markov (Ornstein–Uhlenbeck) process and is therefore ergodic. Physically, this finding is equivalent to stating that vortex meandering is the manifestation of a Brownian motion, as suggested recently by Bölle (2023). This result implies several important corollaries. Probably most notably, experimental vortex meandering corresponds to a linear dynamics for which, due to Gaussianity, no statistical closure is needed. Due to Gaussianity, the standard deviation (meandering amplitude) constitutes a characteristic perturbation scale. Furthermore, the Markov property identifies vortex meandering with a stochastically memoryless process. Our analysis eventually suggests that the characteristic time scale of the meandering dynamics is not a certain period, as thought previously. Rather, the characteristic meandering time scale λ_i^{-1} is a measure of the vortex response, acting to stabilise, or dampen, external excitation. From a practical perspective, the Markov property and λ_i^{-1} also indicate a time scale of predictability, which may be relevant for control applications or wake–vortex encounters in aviation.

Acknowledgements. I would like to acknowledge valuable comments from T. Leweke, S. Le Dizès, V. Brion, A. Stephan and three anonymous reviewers, which helped to improve this paper. I am also grateful to ONERA, the French Aerospace Lab, for providing access to the experimental data.

Declaration of interests. The author reports no conflict of interest.

Author ORCIDs.
Tobias Bölle https://orcid.org/0000-0003-3714-6882.

Appendix. Model–experiment comparison in upstream measurement planes

Other than figure 6, this study focuses on a detailed discussion of the experimental vortex meandering characteristics in a single measurement plane at $z/c = 26$. In this appendix, we show supplementary results from upstream measurement planes at $z/c \in \{2, 4, 12, 20\}$ of the same experiment (§ 2.1) that support the proposed Brownian motion meandering model.

Figure 13 shows that the empirical probability densities are well approximated by a Gaussian distribution (as implied by the model) in all measurement planes. They collapse when standardised, i.e. normalised on the standard deviation, as implied by the theory.

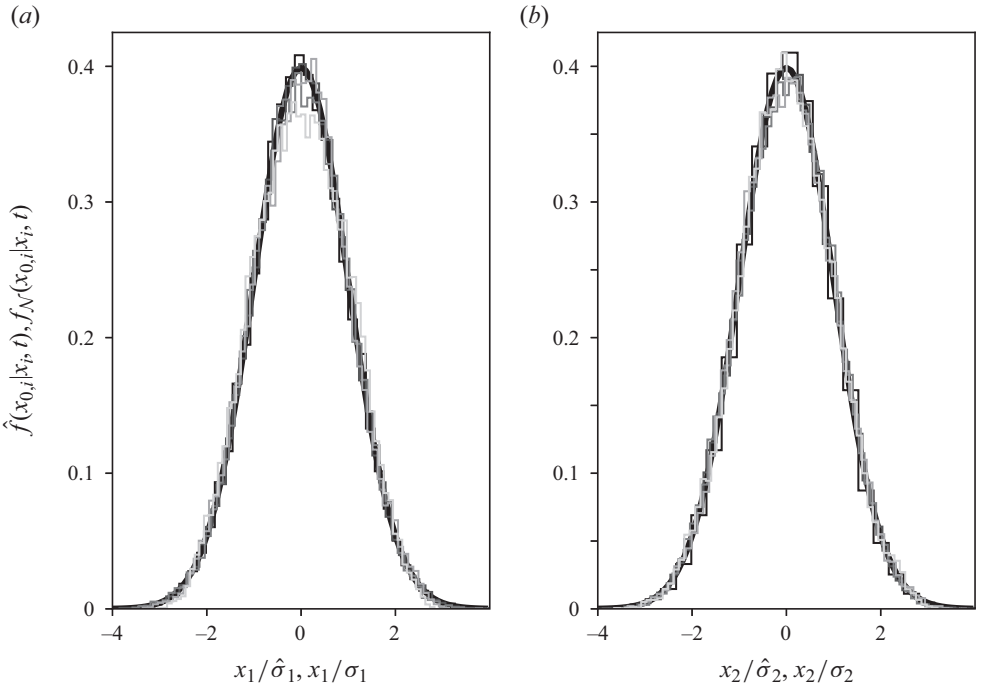

Figure 13. Comparison between the standardised normal probability density $f_{\mathcal{N}}(x_{0,i} \,|\, x_i, t)$ (thick black) with the standardised empirical probability densities $\hat{f}(x_{0,i} \,|\, x_i, t)$, assuming 60 bins: (*a*) first and (*b*) second principal component time series. Progressively lighter grey colour of the histograms corresponds to more downstream measurement planes (see figure 14 for further details).

Figure 14 shows that the empirical power spectra in the last measurement planes ($z/c \gtrsim 10$) collapse when scaled on the local variance level and the integral vortex response time scale. The empirical spectra in the first two planes ($z/c = 2, 4$) qualitatively follow a similar law, but differ quantitatively in the attained variance levels at low frequencies. This difference in the spectral signature seems to be due mainly to the time scale estimates: in the more upstream planes, the dynamics is still close to white noise (flat spectrum). This is consistent with our Brownian-motion-like model. At the same time, it cannot be excluded that other effects not covered by the model contribute to the experimentally observed spectral signature in the first measurement planes. This may be due to the roll-up, transient amplifications, etc. These dynamics are out of the scope of this work.

The spectral trend visible in figure 14 is also consistent with the leading-order vortex response modes. For the given experiment, a dipolar pattern can be identified in the fluctuation vorticity by a POD already in the most upstream measurement plane at $z/c = 2$ that qualitatively is identical to the one shown in figure 3 (Bölle 2021; Bölle *et al.* 2023). The main difference is that, unlike figure 4, this mode contributes only a small fraction to the total variance. Hence, although vortex meandering seems to be present already at the upstream stations ($z/c = 2, 4$), it has an almost white noise signature. The variance then gradually accumulates in the leading POD modes (Bölle *et al.* (2023) and figure 6). This is the essence of a Brownian motion, and is consistent with the power spectral evolution in figure 14.

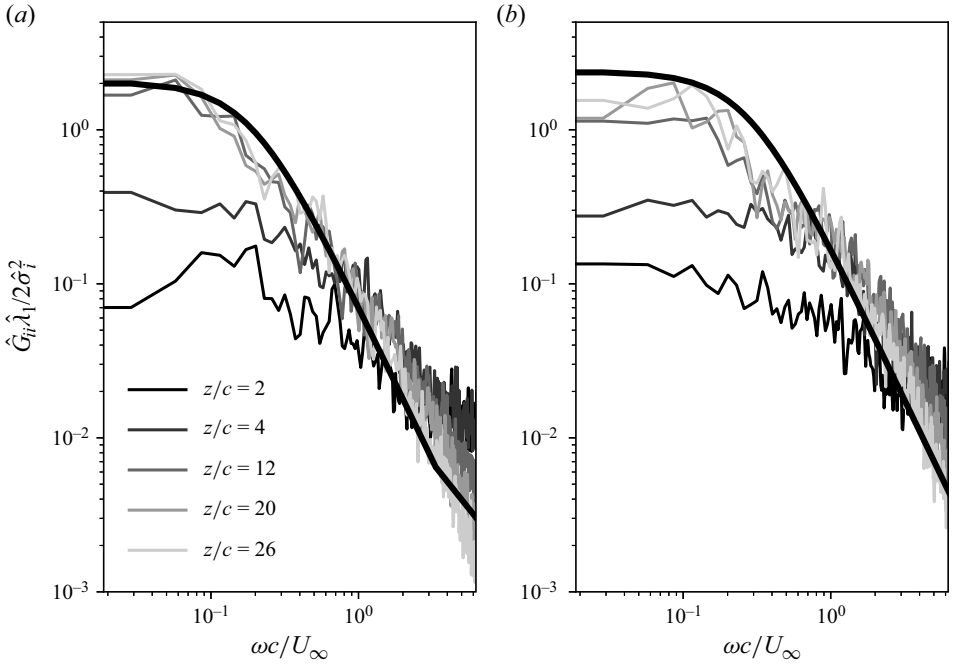

Figure 14. Comparison between the model power spectrum (3.17) (thick black) with the spectral estimates for the (*a*) first and (*b*)second principal component time series.

References

Abraham, B. & Ledolter, J. 1983 *Statistical Methods for Forecasting*. Wiley Online Library.

Antkowiak, A. & Brancher, P. 2004 Transient energy growth for the Lamb–Oseen vortex. *Phys. Fluids* **16**, L1–L4.

Bailey, S.C.C., Pentelow, S., Ghimire, H.C., Estejab, B., Green, M.A. & Tavoularis, S. 2018 Experimental investigation of the scaling of vortex wandering in turbulent surroundings. *J. Fluid Mech.* **843**, 722–747.

Bailey, S.C.C. & Tavoularis, S. 2008 Measurements of the velocity field of a wing-tip vortex, wandering in grid turbulence. *J. Fluid Mech.* **601**, 281–315.

Baker, G.R., Barker, S.J., Bofah, K.K. & Saffman, P.G. 1974 Laser anemometer measurements of trailing vortices in water. *J. Fluid Mech.* **65**, 325–336.

Bandyopadhyay, P.R., Stead, D.J. & Ash, R.L. 1991 Organized nature of a turbulent trailing vortex. *AIAA J.* **29** (10), 1627–1633.

Bartlett, M.S. 1935 Some aspects of the time-correlation problem in regard to tests of significance. *J. R. Stat. Soc.* **98** (3), 536–543.

Bayley, G.V. & Hammersley, J.M. 1946 The 'effective' number of independent observations in an autocorrelated time series. *Supp. J. R. Stat. Soc.* **8** (2), 184–197.

Bendat, J.S. & Piersol, A.G. 2010 *Random Data: Analysis and Measurement Procedures*. John Wiley & Sons.

Bölle, T. 2021 Treatise on the meandering of vortices. PhD thesis, Institut Polytechnique de Paris.

Bölle, T. 2023 On the statistics of coherent vortices in incoherent environments. *Physica* A **612**, 128473.

Bölle, T., Brion, V., Couliou, M. & Molton, P. 2023 Experiment on jet–vortex interaction for variable mutual spacing. *Phys. Fluids* **35**, 015117.

Bölle, T., Brion, V., Robinet, J.C., Sipp, D. & Jacquin, L. 2021 On the linear receptivity of trailing vortices. *J. Fluid Mech.* **908**, A8.

Chandrasekhar, S. 1943 Stochastic problems in physics and astronomy. *Rev. Mod. Phys.* **15**, 1–89.

Corsiglia, V.R., Schwind, R.G. & Chigier, N.A. 1973 Rapid scanning, three-dimensional hot-wire anemometer surveys of wing-tip vortices. *J. Aircraft* **10** (12), 752–757.

Cramér, H. 1963 *Mathematical Methods of Statistics*. Princeton University Press.

DEVENPORT, W.J., RIFE, M.C., LIAPIS, S.I. & FOLLIN, G.J. 1996 The structure and development of a wing-tip vortex. *J. Fluid Mech.* **312**, 67–106.
DGHIM, M., BEN MILOUD, K., FERCHICHI, M. & FELLOUAH, H. 2021 Meandering of a wing-tip vortex in a grid-generated turbulent flow. *Phys. Fluids* **33**, 115131.
EDSTRAND, A.M., DAVIS, T.B., SCHMID, P.J., TAIRA, K. & CATTAFESTA, L.N. 2016 On the mechanism of trailing vortex wandering. *J. Fluid Mech.* **801**, R1.
ENDERS, W. 1995 *Applied Econometric Time Series*. John Wiley & Sons.
FABRE, D. & JACQUIN, L. 2004 Viscous instabilities in trailing vortices at large swirl numbers. *J. Fluid Mech.* **500**, 239–262.
FABRE, D., SIPP, D. & JACQUIN, L. 2006 Kelvin waves and the singular modes of the Lamb–Oseen vortex. *J. Fluid Mech.* **551**, 235–274.
FARRELL, B.F. & IOANNOU, P.J. 1996 Generalized stability theory. Part I: autonomous operators. *J. Atmos. Sci.* **53** (14), 2025–2040.
FONTANE, J., BRANCHER, P. & FABRE, D. 2008 Stochastic forcing of the Lamb–Oseen vortex. *J. Fluid Mech.* **613**, 233–254.
FULLER, W.A. 1996 *Introduction to Statistical Time Series*. John Wiley & Sons.
DE GROOT, S.R. & MAZUR, P. 1984 *Non-equilibrium Thermodynamics*. Dover Publications.
GUTIERREZ-CASTILLO, P., GARRIDO-MARTIN, M., BÖLLE, T., GARCÍA-ORTIZ, J.H., AGUILAR-CABELLO, J. & DEL PINO, C. 2022 Higher order dynamic mode decomposition of an experimental trailing vortex. *Phys. Fluids* **34**, 107116.
HAMILTON, J.D. 1994 *Time Series Analysis*. Princeton University Press.
HÄNGGI, P. & THOMAS, H. 1982 Stochastic processes: time evolution, symmetries and linear response. *Phys. Rep.* **88** (4), 207–319.
HANNACHI, A., JOLLIFFE, I.T. & STEPHENSON, D.B. 2007 Empirical orthogonal functions and related techniques in atmospheric science: a review. *Intl J. Climatol.* **27** (9), 1119–1152.
HART, B.I. 1942 Significance levels for the ratio of the mean square successive difference to the variance. *Ann. Math. Statist.* **13** (4), 445–447.
HOLMES, P., LUMLEY, J.L. & BERKOOZ, G. 1996 *Turbulence, Coherent Structures, Dynamical Systems and Symmetry*. Cambridge University Press.
HUSSAIN, F., PRADEEP, D.S. & STOUT, E. 2011 Nonlinear transient growth in a vortex column. *J. Fluid Mech.* **682**, 304–331.
VAN JAARSVELD, J.P.J., HOLTEN, A.P.C., ELSENAAR, A., TRIELING, R.R. & VAN HEIJST, G.J.F. 2011 An experimental study of the effect of external turbulence on the decay of a single vortex and a vortex pair. *J. Fluid Mech.* **670**, 214–239.
JACQUIN, L., FABRE, D., GEFFROY, P. & COUSTOLS, E. 2001 The properties of a transport aircraft wake in the extended near field: an experimental study. In *39th Aerospace Sciences Meeting and Exhibit*, p. 1038.
JAMMY, S.P., HILLS, N. & BIRCH, D.M. 2014 Boundary conditions and vortex wandering. *J. Fluid Mech.* **747**, 350–368.
KARAMI, M., HANGAN, H., CARASSALE, L. & PEERHOSSAINI, H. 2019 Coherent structures in tornado-like vortices. *Phys. Fluids* **31**, 085118.
LANZANTE, J.R. 2021 Testing for differences between two distributions in the presence of serial correlation using the Kolmogorov–Smirnov and Kuiper's tests. *Intl J. Climatol.* **41** (14), 6314–6323.
LEE, S. & MARCUS, P.S. 2024 Transient growth of a wake vortex and its initiation via inertial particles. arXiv:2402.07469.
LEITH, C.E. 1973 The standard error of time-average estimates of climatic means. *J. Appl. Meteorol.* **12**, 1066–1069.
LILLIEFORS, H.W. 1967 On the Kolmogorov–Smirnov test for normality with mean and variance unknown. *J. Am. Stat. Assoc.* **62** (318), 399–402.
MAO, X. & SHERWIN, S.J. 2012 Transient growth associated with continuous spectra of the Batchelor vortex. *J. Fluid Mech.* **697**, 35–59.
NAVROSE, B.V. & JACQUIN, L. 2019 Transient growth in the near wake region of the flow past a finite span wing. *J. Fluid Mech.* **866**, 399–430.
NORTH, G.R., BELL, T.L., CAHALAN, R.F. & MOENG, F.J. 1982 Sampling errors in the estimation of empirical orthogonal functions. *Mon. Weath. Rev.* **110** (7), 699–706.
QIU, S., CHENG, Z., XU, H., XIANG, Y. & LIU, H. 2021 On the characteristics and mechanism of perturbation modes with asymptotic growth in trailing vortices. *J. Fluid Mech.* **918**, A41.
ROY, A. & SUBRAMANIAN, G. 2014 Linearized oscillations of a vortex column: the singular eigenfunctions. *J. Fluid Mech.* **741**, 404–460.

ROY, C. & LEWEKE, T. 2008 Far-wake. Fundamental research on aircraft wake phenomena: experiments on vortex meandering. *Tech. Rep.* AST4-CT-2005-012238, CNRS-IRPHE.

VON STORCH, H. & ZWIERS, F. 2003 *Statistical Analysis in Climate Research*. Cambridge University Press.

TENNEKES, H. & LUMLEY, J.L. 1972 *A First Course in Turbulence*. MIT Press.

THIÉBAUX, H.J. & ZWIERS, F.W. 1984 The interpretation and estimation of effective sample size. *J. Clim. Appl. Meteorol.* **23** (5), 800–811.

TRENBERTH, K.E. 1984 Some effects of finite sample size and persistence on meteorological statistics. Part I: autocorrelations. *Mon. Weath. Rev.* **112** (12), 2359–2368.

VIOLA, F., ARRATIA, C. & GALLAIRE, F. 2016 Mode selection in trailing vortices: harmonic response of the non-parallel Batchelor vortex. *J. Fluid Mech.* **790**, 523–552.

WANG, Z. & GURSUL, I. 2012 Unsteady characteristics of inlet vortices. *Exp. Fluids* **53**, 1015–1032.

WELCH, P. 1967 The use of fast Fourier transform for the estimation of power spectra: a method based on time averaging over short, modified periodograms. *IEEE Trans. Audio Electroacoust.* **15** (2), 70–73.

WILKS, D.S. 2006 *Statistical Methods in the Atmospheric Sciences*. Academic.

YAGLOM, A.M. 1962 *An Introduction to the Theory of Stationary Random Functions*. Prentice Hall.

ZHANG, H., WANG, H., XU, Z., LIU, Z. & KHOO, B.C. 2023 Investigation of the fluctuating velocity in a single-cell tornado-like vortex based on coherent structure extraction. *Phys. Fluids* **35**, 015135.

ZWIERS, F.W. & VON STORCH, H. 1995 Taking serial correlation into account in tests of the mean. *J. Clim.* **8** (2), 336–351.